Process Safety and Environmental Protection 202 (2025) 107812

Contents lists available at ScienceDirect

Process Safety and Environmental Protection

journal homepage: www.journals.elsevier.com/process-safety-and-environmental-protection

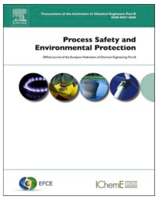

Intelligent performance enhancement of flue gas waste heat recovery in combined low-temperature economizer – Air heater systems

Huaan Li, Dongliang Wei, Yajie Wu, Tianxing Zhou, Hao Zhou *

Zhejiang University, Institute for Thermal Power Engineering, State Key Laboratory of Clean Energy Utilization, Hangzhou 310027, PR China

ARTICLE INFO

Keywords:
Flue Gas Waste Heat Recovery
Capacity Expansion Retrofit
Flue Gas Parameter Prediction
Algorithm Comparison
Optimization Analysis

ABSTRACT

To enhance flue gas waste heat recovery (FGWHR) and address the significant time delay in traditional Proportional-Integral-Derivative control of the low-temperature economizer (LLTE) and air heater (AR) system, a capacity expansion retrofit integrating an air heater (AR) with the LLTE in a 1000 MW coal-fired unit was investigated. The retrofit's effects on key performance indicators, such as thermal efficiency, power generation, and coal consumption, were evaluated. The predictive performances of Backpropagation, Long Short-Term Memory, Temporal Convolutional Network–Transformer, and Least Squares Support Vector Machine models (LSSVM) for flue gas parameters were compared, with the Constrained Particle Optimization (CPO)- LSSVM model achieving the highest accuracy and generalization. By utilizing the predicted flue gas parameters, real-time optimization was carried out through CPO-HYSYS. The thermal efficiency and environmental benefits were both enhanced. It is demonstrated that intelligent algorithms for real-time flue gas prediction and optimization provide an effective solution to overcome lag in FGWHR systems.

ηthermal efficiency

Abbreviations

αi	Lagrange multipliers
CPO	Crested Porcupine Optimizer
d	bias term
e_i	deviation
F_i^t	average force exerted on the i-th predator
FGT	flue gas temperature
FGWHR	flue gas waste heat recovery
$K(x_i, x_j)$	kernel function
L	minimum bound
LLTE	low temperature economizer
MAE	Mean Absolute Error
MAPE	Mean Absolute Percentage Error
MSE	Mean Squared Error
N	population size
r	random number
R^2	R-squared
RBF	Radial function
RMSE	Root Mean Squared Error
S_i^t	the scent diffusion factor
t	current evaluation
T	circular variable
u	uncertainty
U	maximum bound
w	vector of weights
WHR	waste heat recovery
*K*im	the dimensionality of the model's initial input data
Zim	Prediction time
∂	coverage factor
x	Result
γ	regularization parameter
γ_t	defense factor
τ	random number
Ω	matrix
σ	Kernel bandwidth
δ	parameter influencing the search direction
Δ_e	instrument error
$\phi(x)$	nonlinear function

1. Introduction

Global climate change has emerged as an increasingly critical and pressing challenge in recent years. Governments and international organizations have intensified their regulation and reduction requirements for carbon emissions, leading to changes in the energy

---

* Corresponding author.
E-mail address: zhouhao@zju.edu.cn (H. Zhou).

https://doi.org/10.1016/j.psep.2025.107812
Received 4 July 2025; Received in revised form 30 August 2025; Accepted 1 September 2025

Nomenclature

Symbols

b	coal consumptiong/kWh
B_j	coal consumption rate before modificationt/h
c	CO_2 emission reductiont/h
h	enthalpyKJ/kg
h_y	flue gas enthalpyKJ/kg
h_{net}	heating value of standard coalKJ/kg
HR	coal consumption rate in the discharge processt/h
m	flow ratet/h
ΔN	work done by 1 kg of coalMW
Q_c	flue gas waste heat recoveryMW
P	Power outputkW
s	Specific entropyJ/(kg·K)
ξ	Carbon dioxide produced by the combustion of 1 kg of standard coalkg

market. As a result, the utilization of low-temperature waste heat resources has attracted significant attention (Men et al., 2021; Yuan et al., 2023).

Waste heat recovery (WHR) technology is widely used in power generation (Dong et al., 2021), refrigeration (Lu et al., 2019), and heating (Tang et al., 2024). In power generation, the Organic Rankine Cycle (ORC) is considered one of the most representative technologies (Shi et al., 2018). Scholars have made significant progress in various research directions in recent years, especially in mixed working fluid simulation (Abbas and Vrabec, 2021), expansion machine performance, and ORC experimental characteristics (Feng et al., 2023; Lin et al., 2019). However, the efficiency of ORC technology is relatively low when dealing with heat sources below 100°C, making it challenging to utilize it under such conditions effectively. As a result, the application of heat pump technology has been further developed (Qiao et al., 2023). Heat pumps can convert low-grade thermal energy into usable heat for electricity production or heating, and are extensively applied in refrigeration (Tassenoy et al., 2022).

Caliskan et al. (2022) integrated a phase change material (PCM) as the heat transfer medium with an LLTE, ultimately producing hot air via the PCM heat exchanger for building space heating. In this system, the phase change modules within the PCM heat exchanger were heated by the working fluid from the economizer, while the LLTE was driven by flue gas from the building's boiler unit. This approach bridged the research gap between efficient energy utilization in buildings and the application of intelligent materials. Gürel et al. (2024) developed a circulating fluidized bed boiler (CFBB) system for processing poultry manure from chicken farms. By co-firing locally sourced lignite with poultry manure in a self-designed CFBB combustion chamber, the system enabled efficient and environmentally friendly energy recovery. The study ultimately demonstrated that on-site combustion of poultry manure or lignite–poultry manure blends at chicken farms not only significantly reduced pollutant emissions from lignite, but also met thermal energy demands while achieving harmless disposal of poultry processing waste. Gürel et al. (2023) and Gürbüz et al. (2022) experimentally investigated the effect of volume control of PCM storage containers during thermal loading on heat flux, storage capacity, and conversion efficiency. The results provided the first experimental evidence that implementing volume control of PCM containers in a latent heat thermal storage system effectively enhanced heat transfer performance and energy storage capacity. Jiang et al. (2024) developed a supercritical carbon dioxide power cycle (CPC) system for large ships, enhancing efficiency through WHR. The study first established an ideal WHR cycle model to guide the CPC layout. Through multi-objective optimization, the layout scheme with optimal overall performance was identified. Bellos (2024) enhanced the efficiency of a Carnot battery by incorporating Al_2O_3 and Cu nanoparticles into the working fluids, extending the existing ORC thermodynamic simulation model. When the nanoparticle mass fraction reached 10 %, the thermal efficiency attained 9 %, with an output power of 13.4 kW. Jiang et al. (2024) developed a refined Carnot battery architecture by integrating subsystem layout improvements with advanced thermal integration strategies. The results indicated that the optimized system achieved a round-trip efficiency improvement of over 30 % compared to the baseline configuration. The optimal working fluid pair was cis-1,3,3,3-tetrafluoropropene-cis-1-chloro-2,3,3,3-tetrafluoropropene, achieving a round-trip efficiency of 85.2 %.

The application of a low-temperature economizer (LLTE) between the Electrostatic Precipitator (ESP) and desulfurization system in coal-fired units presents clear advantages over traditional flue gas waste heat recovery (FGWHR) methods (Wang et al., 2012b; Wang et al., 2014). This technical approach not only offers ease of engineering implementation and strong system compatibility, but also benefits from a mature technological framework and relatively low investment costs, thereby enhancing its overall feasibility for practical application (Espatolero et al., 2010).

To deal with the excessive flue gas temperature (FGT) arising from the long-term operation of coal-fired plants, Stevanovic et al. (2019), Stevanovic et al. (2014) integrated a high-temperature economizer with an LLTE into a combined system. By utilizing the recovered waste heat to preheat cooling water and secondary air, this configuration significantly reduced coal consumption. Xiao et al. (2019) introduced a bypass-type LLTE setup and found that the bypass ratio played a critical role in its energy-saving capability. The optimal bypass ratio varied under different load conditions and should be adjusted accordingly based on the actual situation. Ma et al. (2021) employed lithium bromide to efficiently recover waste heat through evaporation and condensation processes, using the FGWHR to warm the air and thereby enhance the system's overall energy utilization efficiency.

In terms of engineering validation, Xu et al. (2021) constructed an LLTE experimental setup for a 330 MW unit, providing a comprehensive analysis of how critical parameters such as circulating water flow and vapor-liquid temperature ratio impacted WHR. By implementing a bypass-based staged recovery approach, Yan et al. (2018) effectively lowered the unit's net coal consumption by 5.38 g/kWh. A plant-wide simulation built by Li et al. (2023) in Aspen Plus resulted in 3.69 g/kWh coal savings and 46 t/h of water recovery. Ouyang et al. (2021) realized a tri-generation system of cooling, electricity, and sulfuric acid through FGWHR, improving unit efficiency by 0.64 % while enabling continuous production of 2123 kg/h of industrial-grade sulfuric acid. Zhang et al. (2024) further optimized the FGWHR system, achieving zero liquid discharge of desulfurization wastewater.

Although extensive research has been conducted on LLTE systems, existing studies have primarily focused on novel system designs. Little attention has been paid to the substantial variations in flue gas temperature and velocity during real operation, as well as the LLTE system's nonlinear and delayed responses under changing load conditions. These factors result in suboptimal real-time FGWHR in practical scenarios. With their ability to efficiently extract patterns from large-scale industrial datasets, machine learning algorithms offer practical solutions to the challenges of nonlinearity and long-time delays (Zhang et al., 2022).

Qi et al. (2025) utilized the emission components of solid waste and applied machine learning to predict the variation of component parameters during the flue gas emission process. Their findings demonstrated that the Extreme Gradient Boosting model achieved remarkable predictive accuracy, with Coefficient of Determination (R^2) values exceeding 0.98 for all flue gas component parameters. The Nonlinear Auto Cross Regression (NAXR) and Temporal Convolutional Network (TCN) models were developed by Wang et al. (2024) to predict SO_2 levels after desulfurization based on inlet flue gas data. The results showed that the TCN model achieved a Root Mean Square Error (RMSE) as low as 1.46 %.

The dynamic operation of biomass combined heat and power (bio-CHP) plants leads to significant fluctuations in the flow rate and CO_2 concentration of the flue gas, which in turn affect the performance of post-combustion CO_2 capture systems. To optimize the dynamic operation of CO_2 capture, a real-time forecasting model for flue gas flow and CO_2 levels was developed by Pan et al. (2024). Di Bonito et al. (2023) were the first to combine artificial neural network models with analytical models to predict the SO_2 levels at a ship scrubber outlet. Lu et al. (2021) developed a three-dimensional numerical model combined with Long Short-Term Memory (LSTM) and 3D-var to predict air quality, resulting in a 29.3 % decrease in RMSE. He et al. (2022) studied the changes in fine particulate matter with an aerodynamic diameter of less than 2.5 micrometers levels through multiple linear regression (MLR) analysis combined with the Weather Research and Forecasting model coupled with Chemistry online chemical model.

At the same time, optimizing system operating parameters to ensure the maximum FGWHR remains a significant challenge (Liu et al., 2020; Z. Wang et al., 2017). Coupling intelligent algorithms for optimization has become the key solution to this problem. Singh et al. (2024) designed and optimized a novel solar power generation system by coupling an Artificial Neural Network (ANN) with the Particle Swarm Optimization (PSO) algorithm. Bao et al. (2024) proposed a theoretical and machine-learning model for a fan-radiator-thermoelectric generator system used in WHR. The model was designed to predict the performance of the thermoelectric components, while a Genetic Algorithm (GA) was employed to optimize the maximum power output and the geometric model. Zhao et al. (2021) conducted an optimization design for industry coupling Adsorption Refrigeration Cycle and heat exchanger networks (HEN). Sun et al. (2024) proposed a novel WHR system that integrates Compressed Air Energy Storage, ORC, and HEN. They optimized the operating parameters with total cost and total exergy as objectives, and the results demonstrated a 19.2 % improvement in WHR efficiency. Zoghi et al. (2024) comprehensively analyzed 13 distinct system configurations for WHR, considering energy efficiency, exergy performance, and environmental impact. Using the Technique for Order Preference by Similarity to Ideal Solution method, Tavana et al. (2024) optimized key parameters in a system that recovered waste heat from boiler flue gas for power generation, cooling, and heating applications.

Based on literature, experimental studies on the practical application of LLTE-air heater (AR) coupling retrofit in 1000 MW coal-fired units remain relatively limited. During actual operation under variable load conditions, the flue gas-water heat exchange system in the LLTE exhibits pronounced nonlinear characteristics and time-delay effects, making it difficult for conventional PID control methods to achieve precise regulation. As a result, the effective utilization of flue gas waste heat is hindered. Moreover, research on how to achieve real-time control and optimization of retrofitted units to maximize FGWHR is insufficient. The main research work conducted here is as follows.

Focus is on a 1000 MW supercritical unit, examining the engineering implementation of a combined capacity expansion retrofit involving an LLTE and an AR, thereby providing practical guidance for the utilization of low-temperature flue gas waste heat in coal-fired power plants.

In response to the pronounced changes in FGT and flow rate following the retrofit, predictive intelligent algorithms were employed. Under variable load conditions, the model fully considered the operational characteristics of the unit and performed multivariate time series modeling. The prediction performance of Backpropagation (BP), LSTM, TCN-Transformer, Least Squares Support Vector Machine (LSSVM) algorithms was evaluated using metrics such as Mean Squared Error (MSE), RMSE, Mean Absolute Error (MAE), Mean Absolute Percentage Error (MAPE), and R^2. It was investigated how key parameters affect its predictive accuracy and identified the most effective input features.

To address the lagging behavior observed during the actual operational adjustments of an LLTE system, a coupled LLTE-AR model was established using HYSYS software. The predicted flue gas parameters were used as feedforward inputs and preloaded into HYSYS, where real-time optimization was conducted by integrating the Constrained Policy Optimization (CPO) algorithm. When the boiler load fluctuated, the system's valve positions were pre-adjusted based on forecasted data, allowing the FGT at the LLTE and the air and water outlet temperatures to remain stable. Performance indicators like power output, thermal efficiency, and coal consumption were evaluated before and after the retrofit optimization.

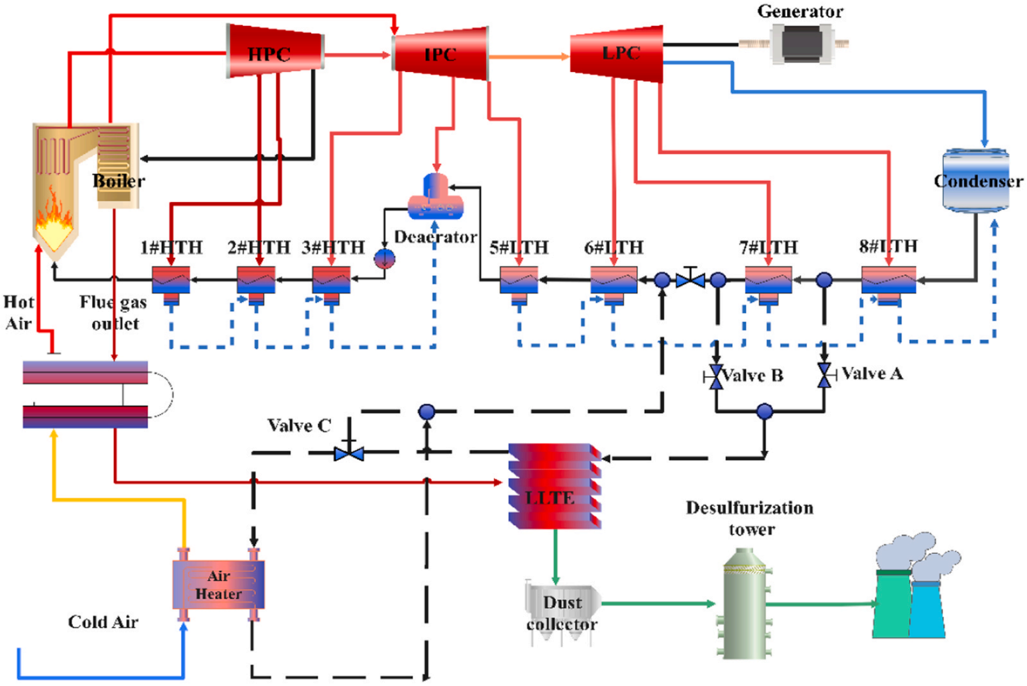

Fig. 1. Capacity expansion retrofit flowchart.

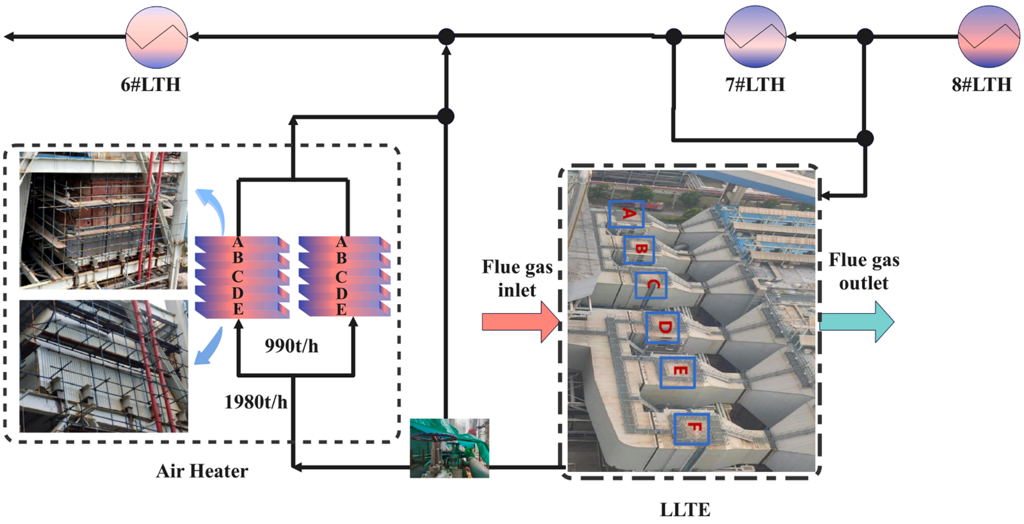

Fig. 2. Experimental device of LLTE and AR.

2. Experimental device

2.1. System configuration

Based on the principle of cascade energy utilization, a boiler FGWHR is commonly employed to reduce stack heat losses. This technology has been widely applied in international engineering practice in various forms, including recovering flue gas heat through waste heat recovery devices to preheat the unit's condensate water; installing a flue gas bypass downstream of the air preheater; and utilizing flue gas waste heat to preheat low-pressure condensate water and the AR simultaneously.

The LLTE technology enables the recovery of flue gas waste heat into the low-pressure condensate side of the turbine regenerative system, thereby increasing the condensate temperature. This process partially displaces extraction steam in the regenerative system, enhances the turbine's power output capability, and improves the unit's thermal efficiency. As a result, it has been widely adopted in domestic power plants.

Installing an LLTE has little impact on the air temperature at the AR outlet. In actual operation, the outlet air temperature often rises slightly due to the concurrent operation of the AR, thereby avoiding any negative effects on the boiler combustion system. Moreover, the LLTE allows flexible control of the FGT at its outlet—slightly lower in summer and slightly higher in winter—effectively preventing low-temperature corrosion of the heating surfaces.

Conventional air heater technology has been applied for many years in flue gas–air systems of coal-fired boilers. Its main feature is extracting a heat source from the system to preheat the cold air at the fan outlet, which effectively increases the average outlet temperature of the AR and prevents low-temperature corrosion of equipment. At the same time, units equipped with air heater technology can avoid the need for hot-air recirculation, thereby ensuring the safe operation of the forced draft fan.

In an FGWHR system where the LLTE operates in conjunction with the AR, the unit uses condensate water from the outlet of a selected low-pressure heater as the heat carrier to recover waste heat from the boiler's tail flue gas. After heat recovery, this condensate water replaces the original heat source for the AR, which can then slightly warm the cold air entering the AR, marginally increasing the air temperature at the preheater outlet. The operation of the AR effectively improves the complex operating environment of the air preheater. At the same time, the modest increase in its outlet FGT helps reduce ammonium bisulfate deposition and blockage on the heating surfaces.

Studies have shown that the application of an LLTE can significantly reduce the flue gas's resistivity due to fly ash, enhance electrostatic precipitator efficiency, decrease water consumption in desulfurization, improve desulfurization performance, and lower particulate emissions. The use of AR, on one hand, can effectively prevent issues such as ammonium bisulfate deposition and ash blockage caused by improper ammonia injection control in the selective catalytic reduction (SCR) system. On the other hand, by raising the boiler's air supply temperature, the operation of the air heater system can also improve overall boiler efficiency.

The experiment focused on a 1000 MW thermal unit retrofitted with an LLTE and a secondary AR, as shown in Fig. 1.

Fig. 1 illustrates the overall retrofit scheme of the LLTE coupled with the AR. In this design, FGWHR was achieved by diverting flow from both upstream and downstream of the 7# LTH into the LLTE system. By adjusting the opening ratios of Valve B and Valve C, the inlet temperature of the LLTE was maintained above 70 °C to prevent low-temperature corrosion. After the LLTE performed low-temperature flue FGWHR, part of the energy was used to heat the secondary air, while the rest was directed back to the 6# LTH. Following the retrofit, a portion of the FGWHR was converted into secondary air energy and returned to the boiler, while the remainder heated water, reducing steam extraction from the 7# LTH—thereby improving the boiler's thermal efficiency.

2.2. LLTE and AR system

Fig. 2 illustrates the installation and structure of the LLTE. Multiple LLTE units were arranged in series along the flue gas flow path in this retrofit. To facilitate installation and maintenance, the rows were grouped into modular structures and assembled on-site. Each module had separate inlet and outlet manifolds, with elbows placed outside the flue duct to avoid intermediate tube welds. Some heat exchanger modules were equipped with manual isolation doors and venting doors on the small inlet and outlet manifolds, aligned with the direction of the flue gas flow. These were designed to isolate circuits in equipment failure, improving the ease of replacement. Under fluctuating loads, it was important to keep the LLTE outlet FGT consistently within the range of 88 °C to 92 °C.

During actual operation, the outlet air temperature was controlled by adjusting the valve opening of the water entering the AR. At design conditions, the AR outlet temperature stayed above 100 ℃. Each unit was equipped with two sets of secondary AR located at the supply fans A and B outlet dampers. The AR was split into five vertical modules, labeled A to E from top to bottom. Detailed structural parameters of the AR and LLTE can be found elsewhere (Li et al., 2025).

Error analysis mainly consists of two parts. The first part pertains to errors arising from directly measured parameters, which include both Type A and Type B uncertainties. Type A uncertainty is based on repeatability and provides an objective and realistic assessment of a physical quantity. It is obtained by performing n independent repeated measurements within a short time, and the experimental standard deviation of the mean, $s(\bar{x})$, is taken as the corresponding uncertainty. The calculation formula is as follows:

$$\bar{x} = \frac{1}{n}\sum_{i=1}^{n} x_n \tag{1}$$

$$u_A = s(\bar{x}) = \sqrt{\frac{1}{n(\mathrm{n}-1)}\sum_{i=1}^{n}(x_i - \bar{x})^2} \tag{2}$$

Type B uncertainty is evaluated based on statistical analysis rather than repeated experiments. It generally accounts only for the uncertainty caused by instrument errors, and is calculated as follows:

$$u_B = \frac{\Delta_e}{\partial} \tag{3}$$

Δ_e represents the instrument error, and ∂ is the coverage factor. When the instrument error follows a normal, uniform, or triangular distribution, ∂ takes the values of 3, $\sqrt{3}$, and $\sqrt{6}$, respectively.

The combined standard uncertainty is obtained by synthesizing Type A and Type B uncertainties. For directly measurable parameters in the experimental setup, such as temperature, pressure, and flow rate, uncertainty analysis can be performed using the combined standard uncertainty.

$$u_C = \sqrt{u_A^2 + u_B^2} \tag{4}$$

For parameters that cannot be measured directly, such as system heat transfer, work output, thermal efficiency, and cost, the calculation of uncertainty involves error propagation. Based on the statistical properties of combined uncertainties, the uncertainty of indirectly measured parameters can be calculated using the following formula (Gürbüz, 2018):

$$u(N) = \sqrt{\left(\frac{\partial f}{\partial x_1}\right)^2 u^2(x_1) + \left(\frac{\partial f}{\partial x_2}\right)^2 u^2(x_2) + \cdots + \left(\frac{\partial f}{\partial x_n}\right)^2 u^2(x_n)} \tag{5}$$

The heat absorption of the LLTE and the waste heat utilization of the AR were determined based on measured pressure, temperature, and flow rate. The increments in thermal efficiency, coal savings, and CO₂ emission reductions were all calculated from the flue gas and air heater heat utilization. The estimated values of LLTE heat absorption and AR waste heat utilization are presented as follows:

3. Model

3.1. Thermodynamic analysis

The boiler efficiency of the modified system (η_g) is given by (Kehlhofer, 1991):

$$\eta_g = \eta_{SG} + \Delta\eta_1 \tag{6}$$

η_{SG} represents the baseline boiler efficiency, while $\Delta\eta_1$ refers to the efficiency increment achieved after the upgrade.

The boiler's thermal efficiency increment is:

$$\Delta\eta_1 = \frac{h_{y1} - h_{y2}}{h_{net}} \tag{7}$$

Before the capacity expansion retrofit, the flue gas enthalpy before entering the desulfurization tower was h_{y1}, kJ/kg; after the retrofit, the flue gas enthalpy before entering the desulfurization tower became h_{y2}, kJ/kg. h_{net} is the heating value, 2.93 × 10^4 kJ/kg.

Table 1
Parameters and performance of measuring devices.

Measurement Instruments	Manufacturer	Measurement Range	Measurement Accuracy
Type E Thermocouple	OMEGA	−200–900℃	±0.5 % of reading
Type K Thermocouple	OMEGA	−200–1200℃	±0.3℃
Type T Thermocouple	NANMAC	−200-+ 350℃	±0.5 % of reading
Temperature Transmitter FLUKE 54 II	FLUKE	−200℃- 1372℃	±0.5 % of reading
Pressure Transmitter	Rosemount	−6.22kPa–6.22kPa	±0.05 % of reading
Digital Power Meter	YOKOGAWA	/	± 0.02 % of reading
Vortex Flowmeter	KROHNE	/	± 1.5 % of reading
Ambient Temperature and Humidity Meter HMI41	VAISALA	0–100 %RH −20~+ 60℃	±0.1 %of reading
Ambient Pressure Gauge DPI740	GE Druck	750–1150 mbar	±0.015 mbar

Table 2
Heat absorption of flue gas and air heater at various load conditions.

Parameters	900 MW	700 MW	500 MW	Unit
LLTE Heat Absorption	73.41 ± 0.09	52.73 ± 0.07	42.06 ± 0.04	MW
AR Heat Absorption	47.59 ± 0.09	39.80 ± 0.11	26.63 ± 0.06	MW

Table 3
Meanings of Eqs. (7)-(9).

Formula / Symbol	Meaning
Q_c	Heat recovered from heating condensate water, kW
B_j	The coal consumption rate before modification, kg/s
η_i	The efficiency of the steam turbine before modification, %
η_{gd}	The pipeline efficiency, %.
η_{SG}	Boiler thermal efficiency before retrofit, %
$N = Q_{net,ar}\eta_{SG}\eta_{gd}\eta_i$	Work output obtained from burning 1 kg of coal in the system before LLTE coupled with AR retrofit, kJ/kg
$(h_{y1} - h_{y2})\eta_{gd}\eta_i$	Incremental work output of 1 kg resulting from the reduction in flue gas loss, kJ/kg
$\frac{Q_c}{B_j}(\eta_i - \eta_{jpl})$	Additional work output from heating feedwater and condensate water, kJ/kg
$(h_{y1} - h_{y2})\eta_{gd}\eta_i - \frac{Q_c}{B_j}(\eta_i - \eta_{jp1})$	Incremental work output on the furnace side caused by AR, kJ/kg

The work done by 1 kg of coal is:

$$\Delta N = (h_{y1} - h_{y2})\eta_{gd}\eta_i - \frac{Q_c}{B_j}(\eta_i - \eta_{jpl}) \tag{8}$$

Q_c represents the FGWHR, kW; B_j denotes the coal consumption rate before modification, kg/s; η_i signifies the efficiency of the steam turbine before modification, %; η_{jpl} stands for the average extraction steam efficiency, %; and η_{gd} indicates the pipeline efficiency, %.

The improvement in thermal efficiency ($\delta\eta_1$) is:

$$\delta\eta_1 = \frac{(h_{y1} - h_{y2})\eta_{gd}\eta_i - \frac{Q_c}{B_j}(\eta_i - \eta_{jp1})}{h_{net}\eta_g\eta_{gd}\eta_i - \frac{Q_c}{B_j}(\eta_i - \eta_{jp1})} \tag{9}$$

With (η_{jp1}) being the extraction steam efficiency (Li et al., 2025). Detailed explanations for each term in Eqs. (7)-(9) are provided in Table 3

The WHR by LLTE is:

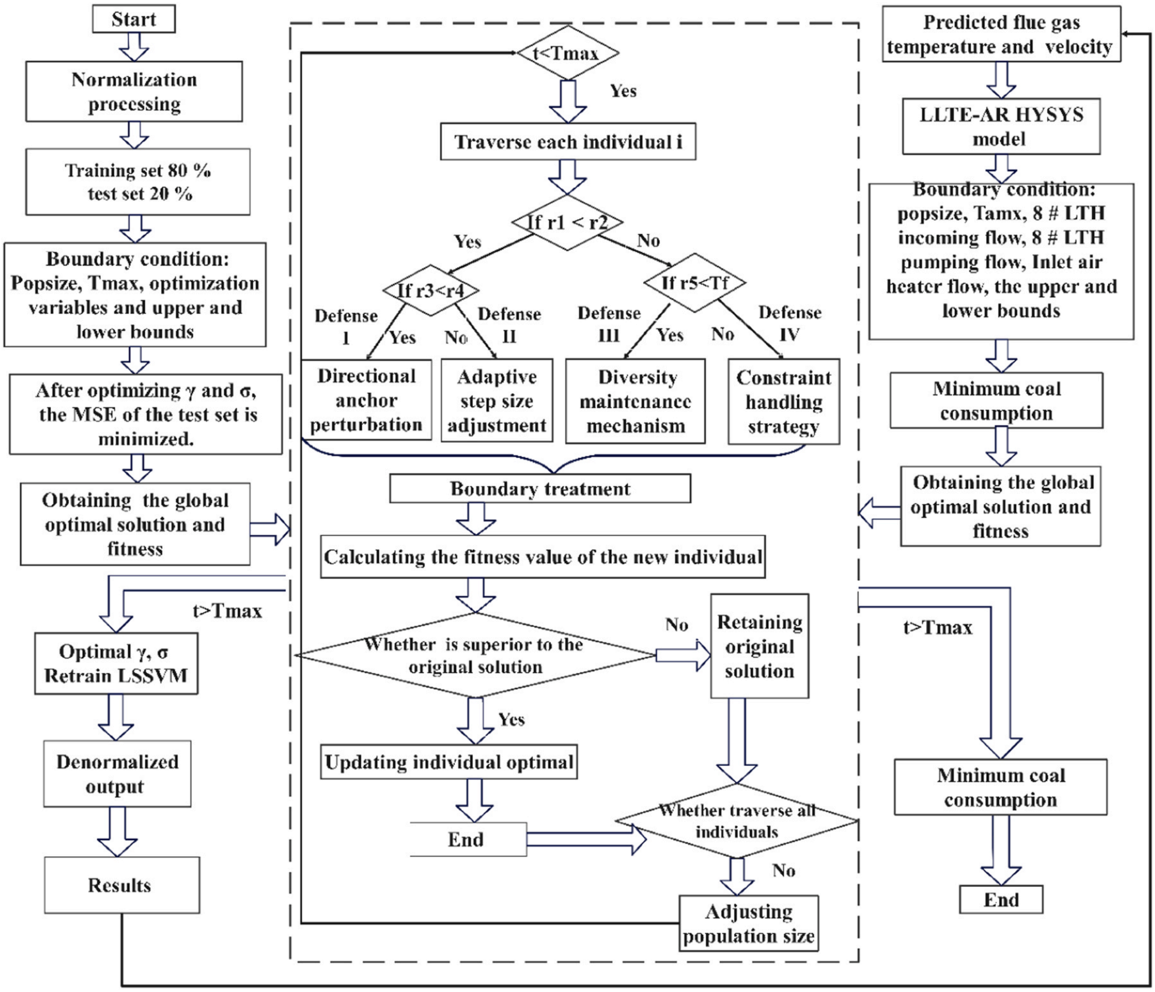

Fig. 3. CPO-LSSVM-HYSYS models.

$$Q_c = m_1(h_2 - h_1) \tag{10}$$

Where, m_1 is the flue gas flow rate, kg/s; h_1 and h_2 are the enthalpy of the hot condensate water at the LLTE inlet and the enthalpy of the feedwater returning to the No. 6 LTH, respectively, kJ/kg.

The WHR by the AR is:

$$Q_f = m_2(h_4 - h_3) \tag{11}$$

m_2 is the air flow rate, kg/s. h_4 represents the specific enthalpy at the outlet of the air heater, kJ/kg; while h_3 denotes the specific enthalpy at the inlet of the air heater, kJ/kg.

Exergy can be expressed as (Wang et al., 2012a):

$$e = h_i - h_0 - T_0(s_i - s_0) \tag{12}$$

h_i is the specific enthalpy of the fluid, kJ/kg; h_0 is the specific enthalpy under the reference ambient condition, kJ/kg; s_i is the specific entropy of the fluid, kJ/(kg·K); s_0 is the specific entropy under the reference ambient condition, kJ/(kg·K); and T_0 is the reference ambient temperature, °C.

The coal-fired heat rate (HR) can be expressed as:

$$HR = \frac{G_{MS} \times H_{MS} + G_{HRH} \times H_{HRH} - G_{FW} \times H_{FW} - G_{CRH} \times H_{CRH} - G_{RH} \times H_{RH}}{P} \tag{13}$$

P is the generator output power, kW; G_{MS}, G_{HRH}, G_{FW}, G_{CRH} G_{RH} are the mass flow rates of the main steam, hot reheat steam, boiler inlet feedwater, cold reheat steam, and desuperheating water, respectively, kg/s; H_{MS}, H_{HRH}, H_{FW}, H_{CRH}, and H_{RH} are the corresponding enthalpies of the main steam, hot reheat steam, boiler inlet feedwater, cold reheat steam, and desuperheating water, respectively, kJ/kg.

The coal consumption for the power supply of the unit (b_1) can be expressed as (Li et al., 2025):

$$b_1 = \frac{HR}{h_{net} \times \eta_{gd} \times (1 - c) \times \eta_g} \tag{14}$$

The reduction value of coal consumption (Δb) can be expressed as:

$$\Delta b = b_0 \times \delta\eta_1 \tag{15}$$

b_0 represents the coal consumption for power generation before the retrofit, g/kWh.

The CO₂ emissions are reduced by (Xiao et al., 2019):

$$c = \frac{\xi \times \Delta b \times P}{1,000,000} \tag{16}$$

Among them, ξ represents the amount of carbon dioxide produced, kg; P stands for the power load, kW.

3.2. LSSVM model

LSSVM is an improved version of the classical Support Vector Machine (SVM), which reformulates the optimization problem by replacing the inequality constraints with equality constraints and minimizing a least-squares cost function. This modification simplifies the computation by solving a set of linear equations instead of a quadratic programming problem, while retaining the advantages of SVM in terms of generalization and robustness (Comak et al., 2007).

The input is nonlinearly mapped to a feature space by $\varphi(x_i)$:

$$f(x) = d + \langle \phi(x), w \rangle \tag{17}$$

The weight vector is denoted by *w*, and the bias term by *d*; the evaluation is formulated as an optimization problem:

$$\begin{aligned} &\min J(w,e) = \min(\frac{1}{2}\|\boldsymbol{w}\|^2 + \frac{1}{2}\gamma\sum_{i=1}^{N} e_i^2) \\ &s.t. y_i = \langle \boldsymbol{w}, \phi(\boldsymbol{x}_i)\rangle + b + e_i i = 1,2,\ldots,N \\ &\gamma > 0 \end{aligned} \tag{18}$$

γ is the regularization parameter balancing model complexity and accuracy, and e_i is the error between predicted and actual values (Kadkhodazadeh and Farzin, 2021).

$$L_{\mathrm{LSSVM}} = \frac{1}{2}\|\boldsymbol{w}\|^2 + \frac{1}{2}\gamma\sum_{i=1}^{N} e_i^2 - \sum_{i=1}^{N}\alpha_i\{\langle \boldsymbol{w}, \phi(\boldsymbol{x}_i)\rangle + d + e_i - y_i\} \tag{19}$$

α_i are the Lagrange multipliers. Eliminating *w* and e_i simplifies the four linear problems to:

$$\begin{bmatrix} 0 & E^{\mathrm{T}} \\ E & \boldsymbol{\Omega} + \frac{1}{\gamma}E \end{bmatrix} \begin{bmatrix} b \\ \alpha \end{bmatrix} = \begin{bmatrix} 0 \\ y \end{bmatrix} \tag{20}$$

$y = [y_1, \ldots, y_n]^{\mathrm{T}}$, $\alpha = [\alpha_1, \ldots, \alpha_n]^{\mathrm{T}}$, and $E = [1, \ldots, 1]^{\mathrm{T}}$. Ω is an $N \times N$ symmetric kernel matrix.

$$\Omega_{ij} = K(x_i, x_j) = \phi(x_i)^{\mathrm{T}}\phi(x_j) i,j = 1,2,\cdots,N \tag{21}$$

$K(x_i, x_j)$ is the kernel function, and the LSSVM model is:

$$y(x) = \sum_{i=1}^{n} \alpha_i K(x_i, x) + b \tag{22}$$

$$K(x_i, x_j) = \exp\left(-\frac{\|x_i - x_j\|^2}{2\sigma^2}\right), \sigma > 0 \tag{23}$$

σ is the kernel bandwidth. The hyperparameters γ and σ greatly influence LSSVM performance (Tresp, 2001).

3.3. *CPO model*

Fig. 3 presents the computational architecture of the CPO-LSSVM-HYSYS algorithms. During the prediction of flue gas parameters using the CPO-LSSVM model, the system initially imported the raw dataset obtained from experimental observations. A nonlinear mapping between the input variables and output responses was then established, and the data underwent standardization pre-processing to enhance model performance. To ensure the robustness and credibility of model validation, a time-series partitioning strategy was adopted: the initial 80 % of the chronological data was allocated for model training. In comparison, the remaining 20 % was retained for evaluating the predictive accuracy. CPO provisioning incorporated four distinct defense mechanisms (Abdel-Basset et al., 2024).

Defense Mechanism I initiated by calculating a central reference point between the current solution and a randomly selected peer, thereby establishing a directional anchor for subsequent position updates. A dynamic perturbation strategy was applied to refine individual positions iteratively. As shown in Eq. (26), this mechanism controls regional transitions. Regions move between the global optimum and the stochastic midpoint. This prevents the algorithm from getting trapped in local optima during the early search stages. By adaptively modulating the exploration trajectory through perturbation vectors, this defense enhanced the algorithm's global search capability and resilience against premature convergence.

Defense Mechanism II was established based on the centroid of randomly selected individuals, with a binary mask U1 applied to enforce dimension-wise selective retention, as delineated in Eq. (27). By incorporating a dynamic perturbation factor, the mechanism maintained the steady-state behavior of critical dimensions while amplifying the global exploration intensity of less active dimensions. This design enables a fine-grained balance between exploitation and exploration at the dimensional level. It enhances the algorithm's adaptability. It also improves search efficiency across diverse optimization landscapes.

An exponentially weighted normalization model, St, was constructed based on population fitness to amplify the guiding influence of superior individuals. As defined in Eq. (28), an iteration-dependent decay-based step size adjustment factor S was introduced to enable a dynamic transition from broad exploratory search in the early stages to fine-tuned exploitation in later iterations. This mechanism employs an inverse operation strategy on the binary mask U1. It preserves information in non-updated dimensions. At the same time, it ensures that the optimization of active dimensions maintains both directional guidance and stochastic variability.

With Defense Mechanism IV, an exponentially amplified fitness-based weighting factor Mt was constructed to achieve nonlinear enhancement of elite individuals' attractiveness, as formulated in Eq. (29). While preserving the diversity safeguard provided by random individual selection, a dual-phase step-size control strategy was introduced. During the early phase, a weighted vector driven by Mt accelerated convergence toward the global optimum region. In the later phase, a reduced step size enabled refined local search within the neighborhood. This dynamic weight adjustment effectively reconciled the trade-off between convergence speed and search precision. Flue gas predictions from the CPO-LSSVM model were fed into the HYSYS simulation in real time.

CPO begins with an initial population of individuals:

$$\vec{X}_i = \vec{L} + \vec{r} \times \left(\vec{U} - \vec{L}\right) | i = 1,2\ldots,N' \tag{24}$$

N is the population size, X_i is the i-th candidate, *L* and *U* are the lower and upper bounds, and *r* is a random variable.

$$N = N_{\min} + (N' - N_{\min}) \times \left(1 - \left(\frac{t\%\frac{T_{\max}}{T}}{\frac{T_{\max}}{T}}\right)\right) \tag{25}$$

T is the total iterations, *t* is the current evaluation, $T_{\max}$ is the maximum, % means remainder, and $N_{\min}$ is the minimum number of individuals.

Defense strategy I: Chaotic sequences are employed to perturb particle positions across regions, enhancing search coverage and preventing premature convergence. It is defined as:

$$\overrightarrow{x_i^{t+1}} = \overrightarrow{x_i^t} + \tau_1 \times \left|2 \times \tau_2 \times \overrightarrow{x_{CP}^t} - \overrightarrow{y_i^t}\right| \tag{26}$$

x_{CP}^t denotes the best solution at evaluation t, y_i^t is the vector from the current to a randomly selected CP in the population, τ_1 is sampled from a normal distribution, and τ_2 is a random number between 0 and 1.

Defense Strategy II: By combining the direction of the global optimum with that of the stochastic midpoint, particles are guided to move differentially within the search space, balancing exploration and exploitation. It is defined as:

$$\overrightarrow{x_i^{t+1}} = \left(1 - \overrightarrow{U_1}\right) \times \overrightarrow{x_i^t} + \overrightarrow{U_1} \times \left(\vec{y} + \tau_3 \times \left(\overrightarrow{x_{r1}^t} - \overrightarrow{x_{r2}^t}\right)\right) \tag{27}$$

r_1 and r_2 are random integers from [1, N], and τ_3 is a random number between 0 and 1.

Defense strategy III: Information in the non-updated dimensions of the binary mask is preserved, while the active dimensions are optimized, maintaining both directional guidance and stochastic variability to

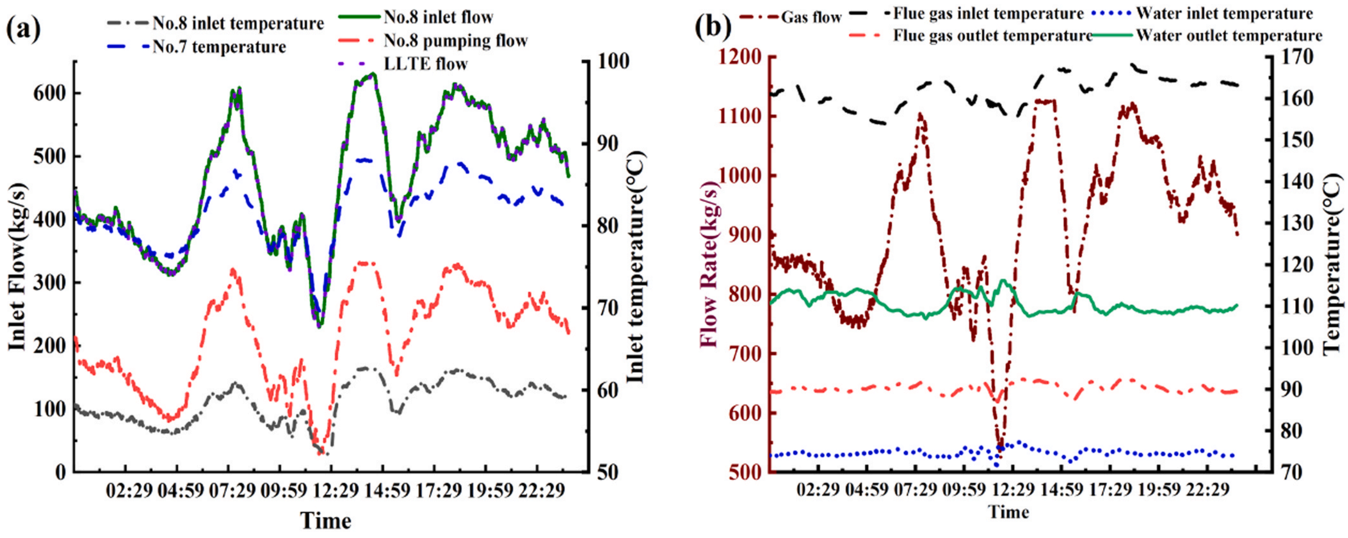

(a) Inlet flow rate and temperature of the LTH

(b) Flue gas flow rate and LLTE water

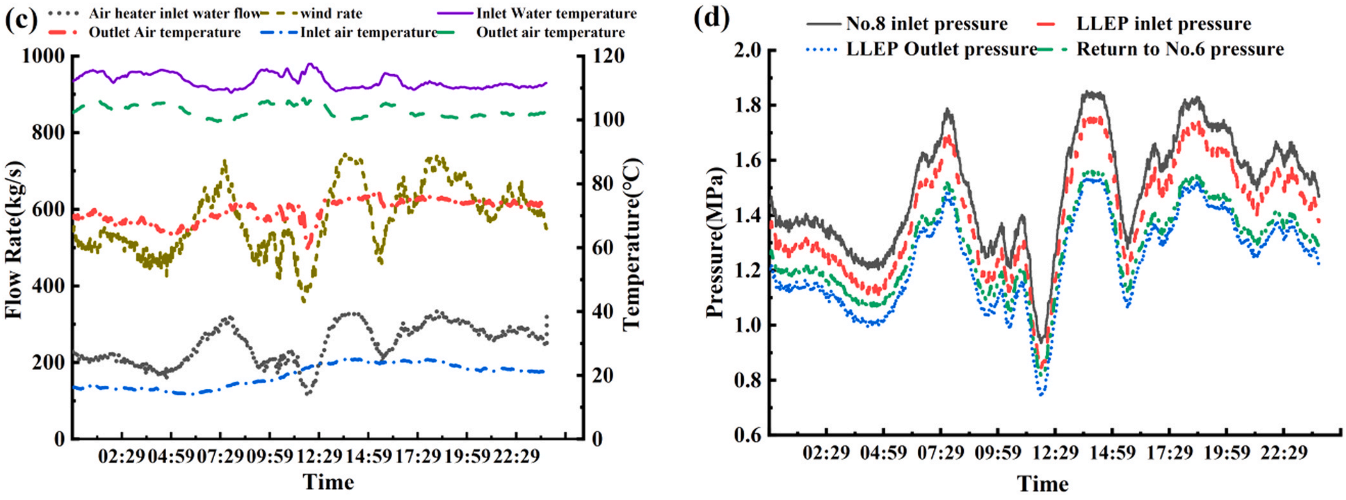

(c) Air flow rate and temperature

(d) Pressure variation

Fig. 4. System parameter changes.

improve search efficiency. It is defined as:

$$\overrightarrow{x_i^{t+1}} = \left(1-\overrightarrow{U_1}\right)\times\overrightarrow{x_i^t}+\overrightarrow{U_1}\times\left(\overrightarrow{x_{r_1}^t}+S_i^t\times\left(\overrightarrow{x_{r_2}^t}-\overrightarrow{x_{r_3}^t}\right)-\tau_3\times\overrightarrow{\delta}\times\gamma_t\times S_i^t\right) \tag{28}$$

r_3 and τ_3 are random variables, δ controls the search direction, x_i^t is the position, γ_t is the defense factor, and S_i^t is the scent diffusion factor.

Defense strategy IV: the weights of different operation layers are adjusted according to the search progress, enabling adaptive switching from broad exploration in the early stages to fine-grained exploitation in the later stages. It is expressed as:

$$\overrightarrow{x_i^t+1} = \overrightarrow{x_{CP}^t}+(\alpha(1-\tau_4)+\tau_4)\times\left(\delta\times\overrightarrow{x_{CP}^t}-\overrightarrow{x_i^t}\right)-\tau_5\times\delta\times\gamma_t\times\overrightarrow{F_i^t} \tag{29}$$

x_{CP}^t is the optimal solution, $x_i^t$is the position of the i-th individual at iteration t, α represents the convergence speed factor, τ_4 is a random value, and F_i^t indicates the average force exerted on the i-th predator by the CP.

4. Experimental

Using the experimental setup, the system's key performance parameters were compared before and after the capacity expansion retrofit. The real-time variations of important parameters throughout the day after the retrofit were explored using varying load conditions as a reference.

4.1. Analysis of performance parameter changes

Fig. 4 presents the dynamic behavior of critical performance parameters within the LLTE system. Across varying load scenarios, substantial changes were observed in flow rate, temperature, and pressure. In Fig. 4(a), the temperature and flow changes between the 7# LTH and 8# LTH showed the same trend, with flow fluctuations being more pronounced than the temperature gradient. During load variation, significant power fluctuations caused instability in the flue gas flow, which in turn led to notable changes in the heat absorbed by the LLTE system.

The detailed variation in flue gas flow over the day is shown in Fig. 4 (b). From 00:00–04:44, the load demand was low, causing the flue gas flow to decrease gradually, reaching a minimum value of 748 kg/s.

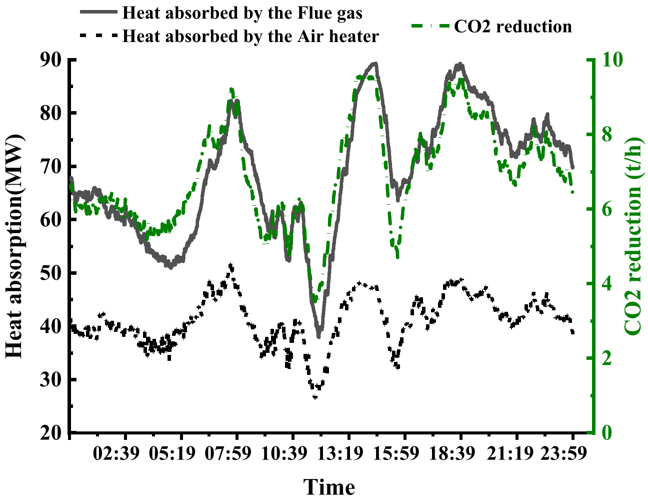

Fig. 5. Energy and carbon reduction variations.

Between 05:00 and 07:42, the flue gas flow continuously increased, peaking at 1106 kg/s. At 11:51, the flow reached its lowest point of 526 kg/s. Afterward, a load adjustment was made, and by 14:02, the flow peaked again at 1125 kg/s. The flow gradually decreased, reaching 771 kg/s at 15:38, followed by fluctuations during high-load operation. The pressure changes shown in Fig. 4(d) and the airflow changes in Fig. 4(c) followed the same pattern of variation.

During operation under varying loads, the flue gas inlet temperature fluctuated between 154°C and 168°C, while the outlet temperature remained between 88°C and 92°C to prevent low-temperature corrosion. The inlet air temperature varied between 14.14°C and 25.22°C. According to the specifications, the AR's outlet temperature needed to exceed 100℃, while the temperature at the LLTE inlet should remain above 70°C.

When the water temperature fell below 70°C, dissolved oxygen, carbon dioxide, and other substances in the water led to condensation, and the acidic condensate could potentially corrode metal surfaces, particularly the internal metal components of the LLTE. Therefore, the water temperature must be maintained above 70°C to prevent condensation and corrosion.

4.2. Analysis of waste heat utilization

Fig. 5 illustrates the changes in WHR and the reduction in CO_2 emissions following the installation of the LLTE system. The WHR by the flue gas and AR was primarily determined by the temperature difference between its inlet and outlet and the gas flow rate. Consequently, the heat absorption variation mirrored the trends observed in the flue gas flow and the quantity of heat transfer fluid supplied to the AR, as illustrated in Fig. 4.

After installing the LLTE system, the flue gas emission temperature was lowered, resulting in reduced fuel consumption, decreased CO_2 emissions, and lower cooling water usage. It is also evident that the CO_2 emission reduction followed the same trend as the FGWHR. According to Eq. (11), CO_2 reduction was primarily driven by coal savings and output power. Under high-load conditions, the greater the WHR, the more coal was saved, leading to more significant reductions in CO_2 emissions.

As shown in the figure, the maximum CO_2 emissions reduction was 9.56 t/h, while the minimum was 3.51 t/h, corresponding to approximately 92.68 % and 34.03 % of the rated operating conditions, respectively. The maximum flue gas and AR WHR were 89.34 MW and 51.94 MW, respectively, with minimum values of 37.92 MW and 26.52 MW.

The integration of the LLTE enabled full utilization of flue gas waste heat, thereby enhancing unit performance. Stevanovic et al. (Stevanovic et al., 2014) retrofitted a 620 MW coal-fired unit with an economizer, recovering 30 MWe of flue gas waste heat and improving the overall efficiency by 0.53 %, which was equivalent to an additional 9.4 MWe of power output. They further evaluated the impact of installation locations. They confirmed that placing the LLTE between the desulfurization tower and the ESP yielded the best performance, which is consistent with the retrofit scheme adopted in this study (Stevanovic et al., 2019).

Fig. 6 shows the real-time changes in thermal economics. As seen from the power variation curve in Fig. 6(a), the overall load fluctuated significantly, with a minimum of 466 kW and a maximum of 1002 kW. Notably, fluctuations in $\delta\eta_1$ and work per kg of coal closely followed changes in output power. As shown in Eqs. (8) and (9), higher power output raised WHR and flue gas enthalpy difference, leading to more incremental work and improved thermal efficiency. In this context, the increase in coal thermal consumption rate and the maximum additional work done by 1 kg of coal were 113.89 kJ/kg and 0.945 %, respectively.

Fig. 6(b) illustrates the variations in coal consumption and coal

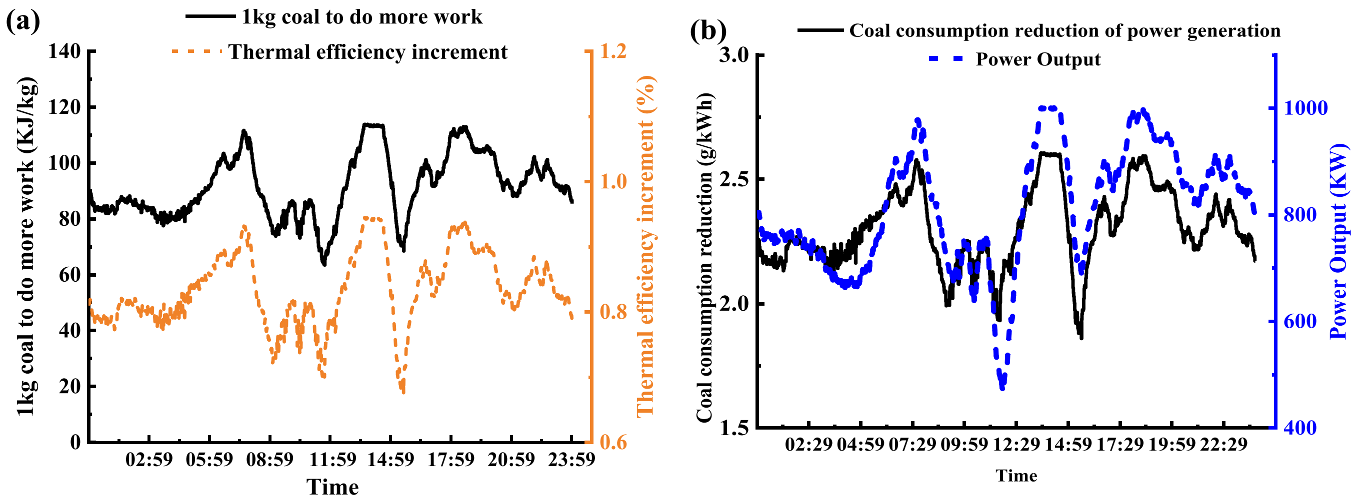

(a) Variation in work output and thermal efficiency

(b) Coal savings and power output variation

Fig. 6. Analysis of thermal economic variations.

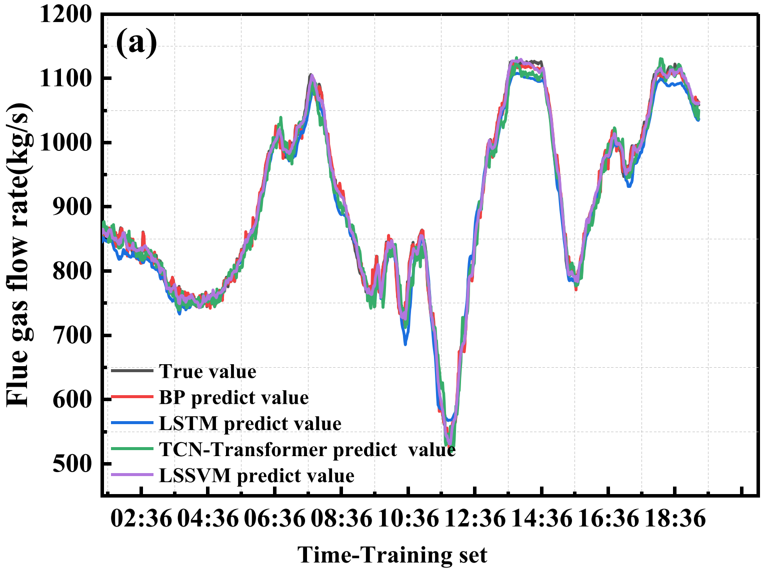

(a) Comparison of flue gas flow rate results in the training set

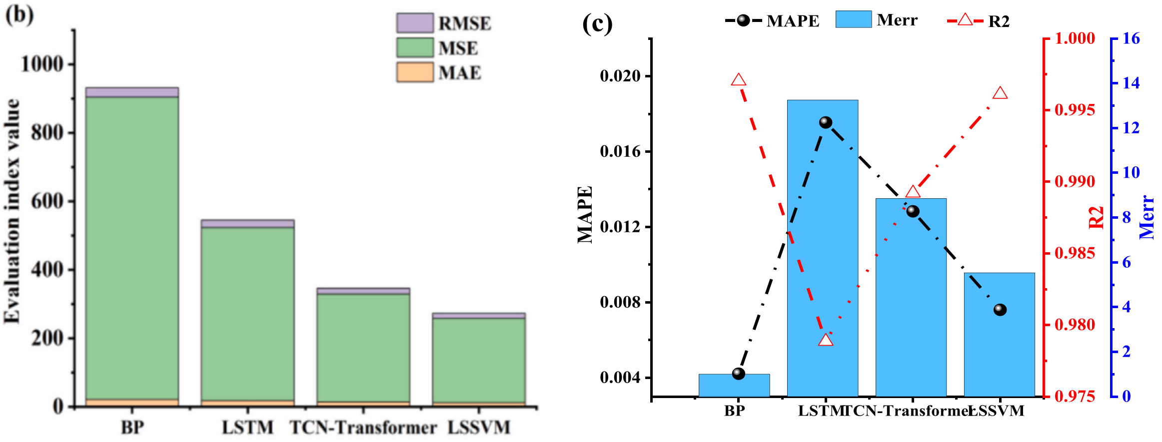

(b) Variations in RMSE, MSE, and MAE

(c) Variations in MAPE Merr and R^2

Fig. 7. Training set results and parameter comparison.

savings. According to Eq. (14), the heat rate was positively correlated with the coal consumption of the power supply and was essentially inversely proportional to the load. At 11:51, the output power dropped to its lowest value of 466.04 kW, resulting in the highest coal consumption and the lowest coal savings. During this period, the maximum coal savings occurred at 13:50, with a corresponding value of 2.61 g/kWh, approximately 97.7 % of the rated operating condition.

Coupling an LLTE with an AR for capacity expansion retrofits in coal-fired power plants yields substantial benefits. At present, many coal-fired units have undergone similar retrofits and reported findings consistent with those of this study. For example, Wang et al. (2012a) evaluated a 600 MW coal-fired unit and assessed the benefits of the LLTE system in terms of energy saving, water conservation, and CO_2 emission reduction. Their results showed that, under full-load operation, the system achieved coal savings of 2 g/kWh, water savings of 25 t/h, and corresponding reductions in CO_2 emissions. Likewise, Xiao et al. (2019) analyzed a 600 MW ultra-supercritical coal-fired unit and examined the effects of the LLTE-AR coupling system on coal savings. Compared with a standalone LLTE system, the improved economizer system further reduced the standard coal consumption rate by 1.1 g/kWh.

5. Comparison of flue gas parameter prediction

Following the capacity expansion retrofit, the LLTE flue gas-water heat exchange system experienced significant time delays and nonlinear behavior under fluctuating load conditions. Conventional PID control approaches were insufficient for achieving accurate regulation. Therefore, an intelligent vector regression model was needed to predict LLTE inlet flue gas parameters in real time using boiler combustion data. This prediction enabled feedforward control, allowing system valves to adjust proactively and keep LLTE flue gas, air, and water temperatures stable during boiler load changes.

To ensure that the experimental data met the algorithm's requirements, the test data from 00:00 on March 29, 2024, to 00:00 on March 30, 2024, was selected as input. The collected data had a time interval of 1 min, resulting in a total of 1441 consecutive time series data points. Various factors influenced the flue gas parameters at the LLTE inlet. Based on actual operating conditions and boiler process requirements, a total of 35 feature variables were extracted, the specific characteristic parameters can be found elsewhere (Li et al., 2025).

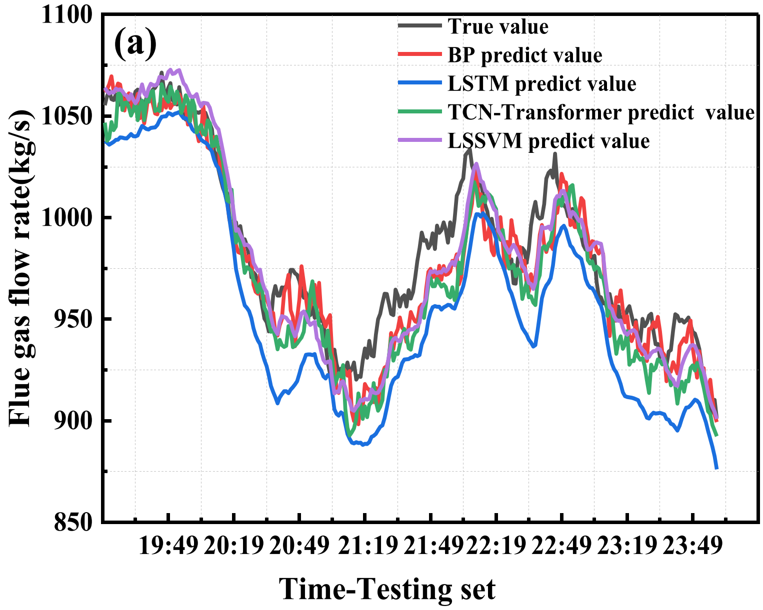

(a) Comparison of flue gas flow rate results in the Testing set

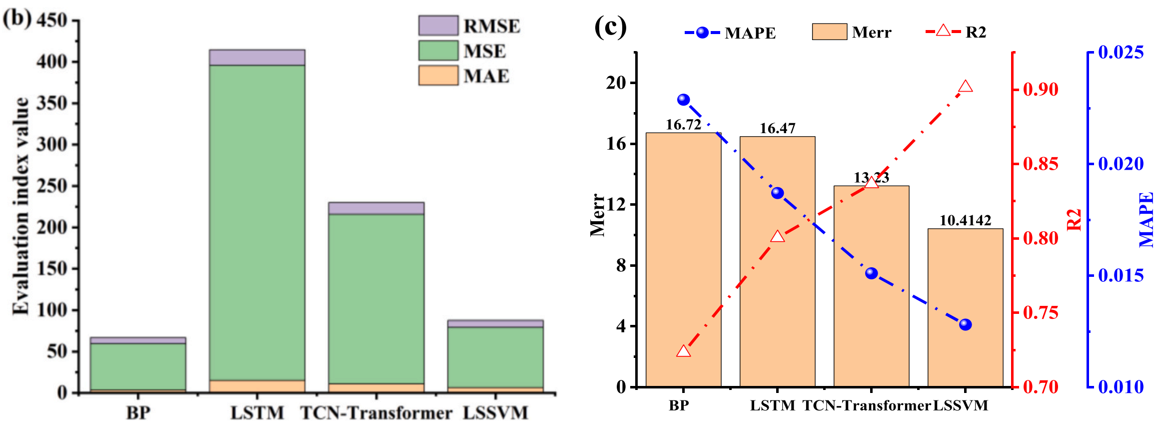

(b) Variations in RMSE, MSE, and MAE

(c) Variations in MAPE Merr and R^2

Fig. 8. Testing set results and parameter comparison.

5.1. Comparison of different algorithms

To assess the accuracy of flue gas parameter predictions, the flow rate was used as the reference, and the prediction results of four different algorithms—BP, LSTM, TCN-Transformer, and LSSVM—were compared.

Due to the varying units of the collected variables and the large differences in their value ranges, model accuracy was adversely affected. To eliminate dimensional inconsistencies among variables, all data were normalized before modeling. Each feature was scaled to the [0, 1] range using the min-max normalization method (Li et al., 2025). To assess the four algorithms, metrics like MSE, RMSE, MAE, MAPE, R^2, and median error (Merr) were applied to both training and testing sets.

The hardware configuration influenced the computational performance. All simulations were conducted on a workstation equipped with a 13th Gen Intel® Core™ i7-13700F processor (2.10 GHz), 32 GB DDR4 memory, and an NVIDIA GeForce GTX 1660 SUPER graphics card. Each algorithm's accuracy was evaluated using the average results from 20 runs.

Fig. 7 comprises the prediction results for the training set using the four different algorithms. In Fig. 7(a), it is evident that LSTM and TCN-Transformer exhibited significant lag in predicting flue gas flow rate, while BP and LSSVM outperformed LSTM and TCN-Transformer. LSTM performed the worst across all metrics, with MAE, MAPE, MSE, RMSE, and Merr reaching 15.203, 0.017, 380.74, 18.82, and 13.255, respectively. Both BP and LSSVM showed similar trends across all metrics, with BP slightly outperforming LSSVM.

The key feature of LSTM was its ability to retain or discard information while preserving memory states selectively. Irrelevant information was discarded during propagation, which helped address the long-term dependency problem in recurrent neural networks. However, the training process of LSTM was relatively complex, which resulted in a delayed response to sudden changes or short-term fluctuations. Additionally, LSTM struggled with processing information over longer time intervals, leading to lower accuracy in results. It still faced long-term dependencies and the vanishing gradient problem. TCN-Transformer combined the strengths of temporal convolution and Transformer models, enabling efficient handling of long time-series data. However, it

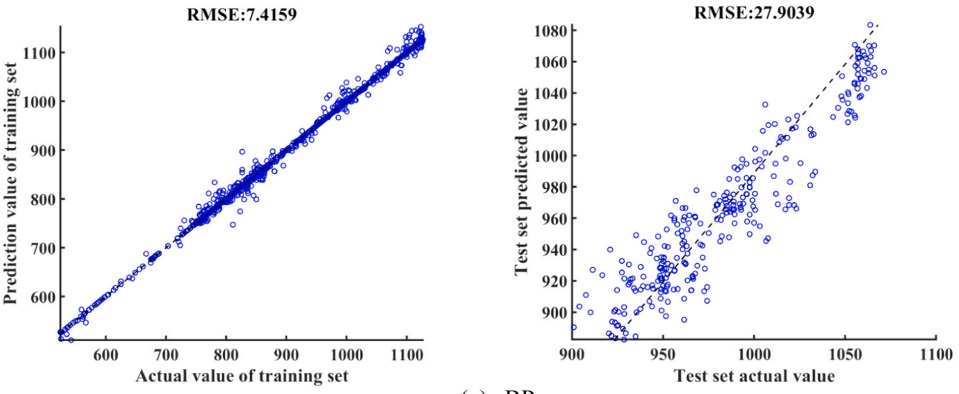

(a) BP

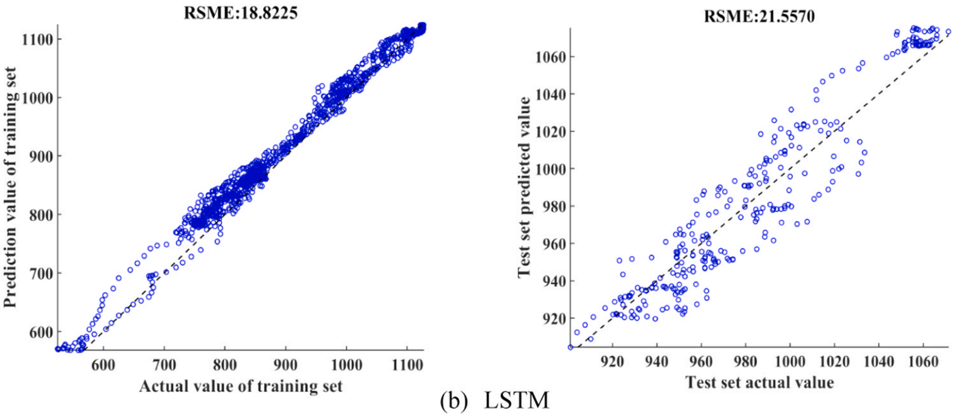

(b) LSTM

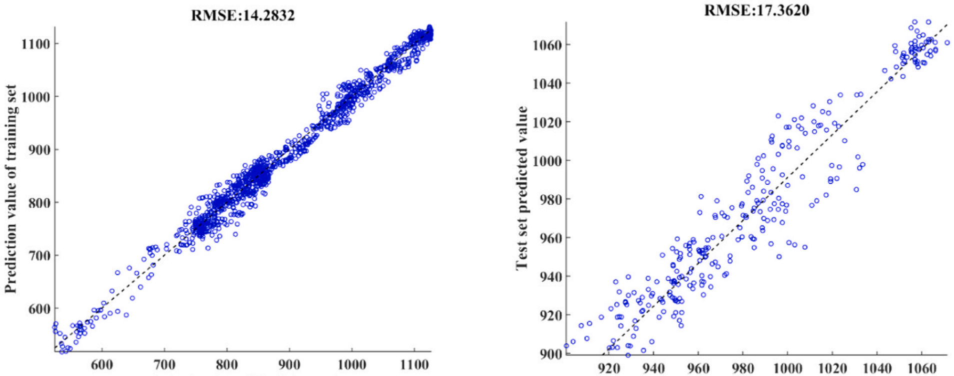

(c) TCN-Transformer

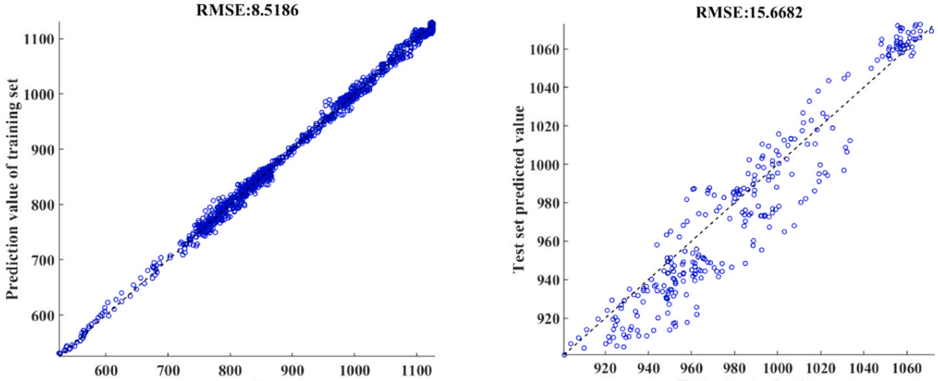

(d) LSSVM

Fig. 9. Comparison of regression performance on training and test sets.

exhibited lag in the short term due to an over-reliance on historical data. Additionally, it had some drawbacks, including relatively low parameter efficiency, sensitivity to input data, and difficulty in processing spatio-temporal dynamic changes.

Comparing the four algorithms, TCN-Transformer, BP, and LSSVM all achieve R^2 values above 0.99, demonstrating good performance, while LSTM has an R^2 value of 0.978, indicating relatively poorer fitting results. Overall, TCN-Transformer, BP, and LSSVM perform exceptionally well in predicting flue gas flow in the training set, with quick responses and good adaptability to changes in the data.

Fig. 8 shows the testing set results and a comparison of parameters. All four algorithms followed a general trend in the variation of flue gas flow rate over time, demonstrating a certain level of generalization capability. Notably, before 20:35, the LSSVM and TCN-Transformer models closely aligned with the experimental flow values, while the LSTM model's predicted flow was noticeably lower. After that point, all four algorithms showed some deviation from the actual flow values, with the BP model exhibiting greater volatility.

Although the BP model showed good predictive performance on the training set, it had certain limitations. It faced a conflict between learning rate and stability, making it prone to getting stuck in local minima during training, which resulted in overfitting. Overfitting degraded the algorithm's performance, leading to strong results on the training data but poor generalization. Additionally, determining the optimal number of neurons in the hidden layer was difficult, and this parameter considerably impacted the prediction outcomes (Sang, 2021).

Comparing Fig. 8(b) and Fig. 8(c), it is evident that the LSSVM and TCN-Transformer models outperformed the BP and LSTM models, with LSSVM showing the best predictive performance. Due to its efficient computational performance and excellent ability to model nonlinear relationships, the LSSVM model achieved the best fit and the smallest error metrics, with MAE, MAPE, MSE, RMSE, R^2, and Merr values of 12.34, 1.28 %, 245.50, 15.67, 0.90, and 10.41, respectively.

Fig. 9 compares the regression performance of the four algorithms on the training and test sets. For the test set, the LSSVM model achieved the lowest RMSE of 15.67, whereas the BP model exhibited the highest RMSE of 27.90. The solid diagonal line represents perfect prediction, with data points near this line indicating better model performance. The LSSVM model aligned closely with the measured values in the regression plot, indicating its high accuracy in predicting flow rate. The BP model was very close to the diagonal line on the training set. The RMSE of the training set reached 7.42, which is significantly lower than that of the LSTM, TCN-Transformer, and LSSVM models. Still, due to overfitting on the test set, the model exhibited significant deviations with more scattered data points and greater volatility, resulting in an RMSE of 27.90.

The LSTM model exhibited considerable prediction bias, particularly in areas with strong lag effects, where data points deviated significantly from the predicted line. Accordingly, the RMSE values for both the training and test sets were relatively poor, amounting to 18.22 and 21.56, respectively.

The TCN-Transformer model was slightly farther from the diagonal line than the LSSVM, approaching the perfect prediction line. However, the data points were more scattered, especially in extreme values or regions with rapid changes, where the predictions showed some deviation. Taking the test set as an example, the RMSE value was 17.36, exceeding the 15.67 observed for the LSSVM model.

In LSSVM modeling, choosing the kernel function and its parameters affected accuracy. Although there is no fixed standard, many studies show that the Gaussian RBF kernel works well. RBF kernel modeling requires choosing suitable values for the regularization parameter (γ) and kernel width (σ), as they directly affect the LSSVM model's learning and generalization.

Kadkhodazadeh and Farzin (2021) employed an LSSVM model optimized by the Gradient-Based Optimizer algorithm to evaluate water quality parameters and demonstrated its superior performance compared with ANN and Adaptive Neuro-Fuzzy Inference System models. Chen et al. (2023) proposed a fatigue monitoring and detection (FMD) model based on an integrated machine learning approach, namely a LSSVM optimized by the Marine Predators Algorithm (MPA). The proposed model was able to capture miners' fatigue states effectively. Compared with conventional Support Vector Machine and LSSVM models, the MPA-LSSVM-based FMD model achieved significantly higher recognition accuracy—by 13.99 % and 18.68 %, respectively—and exhibited superior robustness.

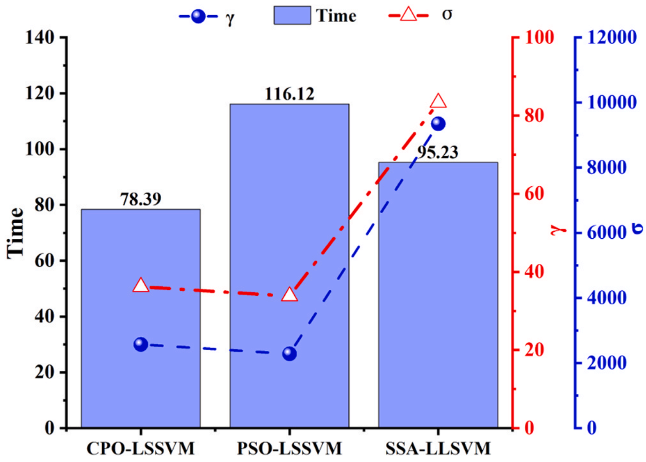

Fig. 10. Parameter optimization and running time.

To establish an accurate LSSVM prediction model, optimizing γ and σ is essential to find the best parameters that balance error and generalization ability. Based on this, the CPO, PSO, and Sparrow Search Algorithm (SSA) algorithms were employed to optimize the γ and σ, thereby improving the accuracy of the prediction model.

Fig. 10 comprises the optimized parameters and runtime for three different algorithms. With the same Zim and Kim values, it is evident that after optimization, the runtime of CPO-LSSVM was only 78.39 s, significantly lower than the 116.12 s for PSO-LSSVM and 95.23 s for SSA-LSSVM.

The significant time advantage of CPO-LSSVM was attributed to the efficiency of the CPO algorithm in both global search and local optimization. It performed effective global searches quickly while avoiding local optima, thereby improving optimization efficiency and significantly reducing the time required. Since the predicted parameters needed to be input into HYSYS for optimization and needed to meet the power plant's operational optimization requirements, CPO-LSSVM was chosen for predicting flue gas temperature and flow.

In this study, the Constrained Particle Optimization (CPO) algorithm was chosen due to its strong capability to handle complex nonlinear constraints, thereby ensuring feasible solutions throughout the search process. Compared to the SSA and PSO, CPO adaptively balances global exploration and local exploitation, which helps avoid premature convergence common in SSA and PSO. It also achieves faster and more stable convergence, is less sensitive to parameter settings, and better suits high-dimensional, constrained problems typical in energy systems.

5.2. Impact of key parameters on CPO-LSSVM

Fig. 11 shows the impact of Kim, Zim, and the proportion of the training set on the CPO-LSSVM prediction results. Kim defined the dimensionality of the model's initial input data, while Zim represented the prediction horizon. As Kim increased, more initial input features were included. While adding more input features may improve the model's representational ability to some extent, an excessive number of features can make the model more complex and increase the computational load, resulting in longer runtime.

As shown in Fig. 11(a), when the training set proportion was kept at

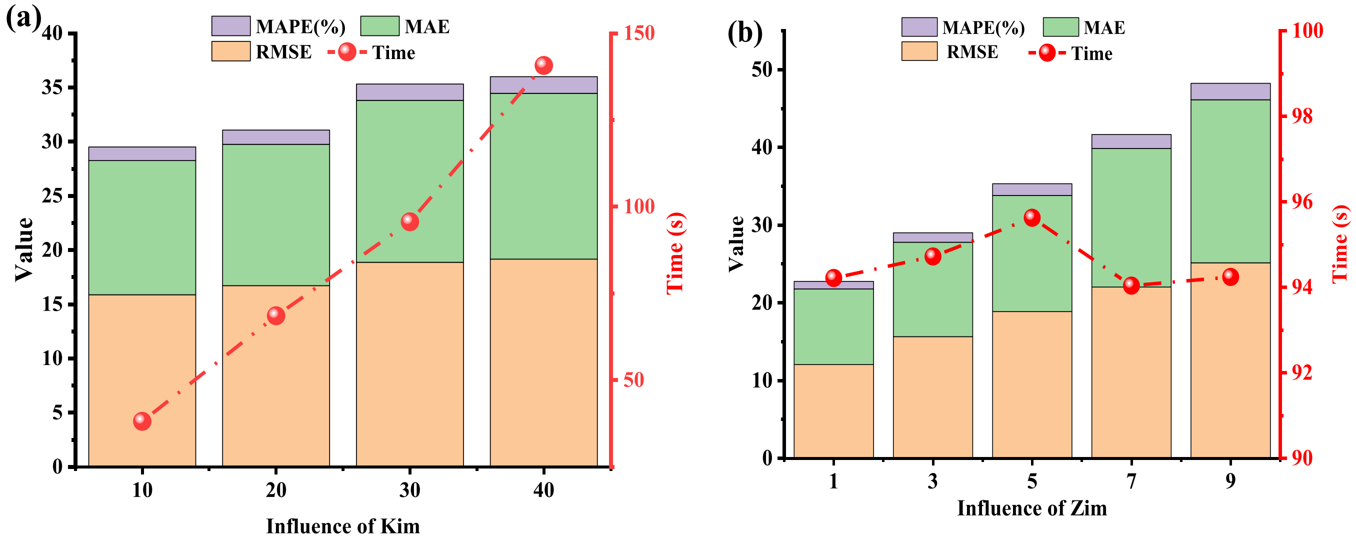

(a)Influence of Kim (b)Influence of Zim

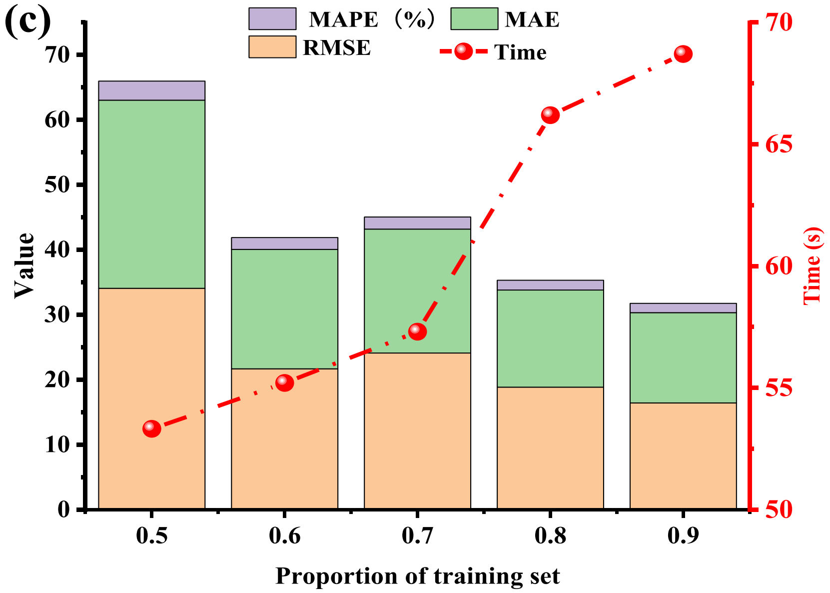

(c) Influence of training set

Fig. 11. The influence of key parameters on CPO-LSSVM.

0.8 and Zim was set to 5 min, the error and runtime gradually increased as Kim increased. In Fig. 11(b), when Kim was fixed at 30, and the training set proportion was 0.8, it can be seen that as Zim increased, the runtime remained relatively constant at around 94.5 s, but the error values rose rapidly. When Zim was 9, the values of RMSE, MAE, and MAPE were more than double those observed when Zim was 1. In Fig. 11 (c), with Kim set to 30 and Zim to 5, increasing the training set proportion led to a gradual decline in overall error, while the runtime correspondingly grew. With 90 % of the data used for training, the RMSE, MAE, MAPE, and computation time were 16.43, 13.88, 1.43, and 68.7 s, respectively.

A moderate amount of training data can help avoid overfitting while improving the model's generalization ability. In Fig. 11(c), the error values were slightly higher when the training set proportion was 0.7 compared to 0.6. Thus, to balance prediction accuracy and timeliness, Kim = 10, Zim = 3, and a training set proportion of 0.8 were chosen for the prediction.

Fig. 12 shows the prediction results of CPO-LSSVM for FGT. After optimization, the model demonstrated accurate generalization ability for the training and test sets. For the FGT test set, MAE, MAPE, MSE, RMSE, and Merr were 0.1014, 0.06 %, 0.0167, 0.1294, 0.9755, and 0.0871, respectively.

For FGT, the lower RMSE obtained with the CPO-LSSVM model further indicates its better accuracy and stability in capturing temperature variations. Compared to other models, it more reliably supports subsequent optimization processes.

In addition to predicting temperature and flow, the proposed system can also be extended to forecast emissions or other pollutants, such as NO_x, SO_2, or CO_2. Based on a data-driven modeling approach, the framework is flexible and scalable. Given sufficient historical operational data—including relevant environmental indicators—the model can be retrained or expanded to include these additional outputs. Such

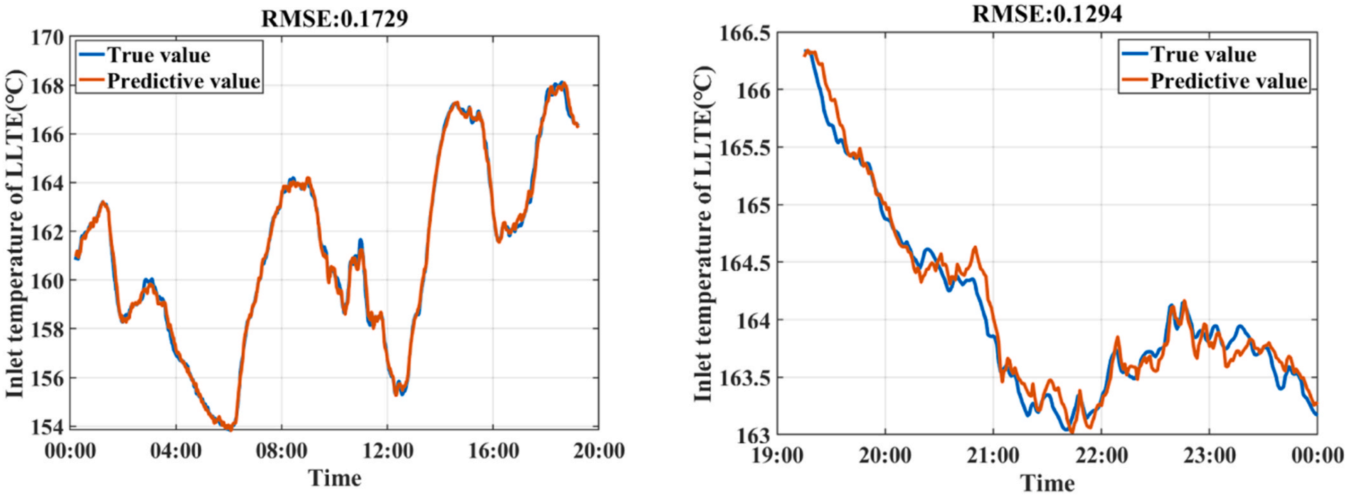

(a) Training set temperature

(b) Test set temperature

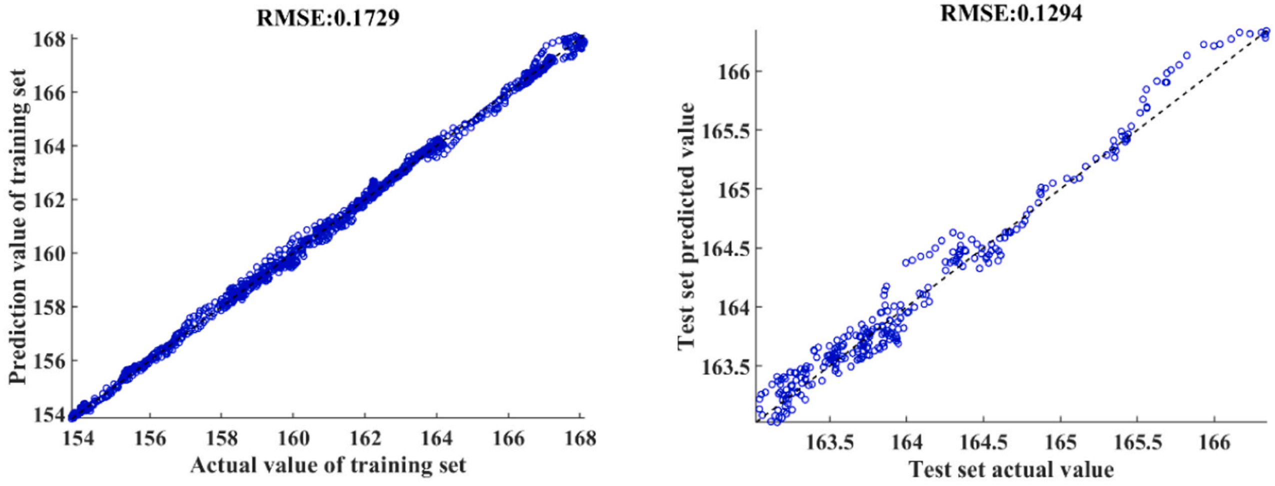

(c) The regression of training set

(d) The regression of test set

Fig. 12. Prediction of FGT by CPO-LSSVM.

an extension would further support intelligent emission reduction and optimization of environmental performance.

6. Optimization analysis

When the boiler load changes, the valve openings of the 8# LTH flow rate, 7# LTH pumping flow, and air heat inlet water flow rate can be adjusted to ensure the maximum FGWHR. Accordingly, the CPO-HYSYS system was employed for optimization, where predicted data were transmitted to HYSYS in real time to regulate FGT, thereby ensuring the maximum FGWHR.

Fig. 13 shows the flowchart of the CPO algorithm coupled with HYSYS and model verification. Fig. 13(a) depicts the LLTE model, and Figs. 13(b) - 13(d) show a comparison between the experimental results and the simulation for this operating condition.

The real-time experimental data of flue gas temperature and flow rate, air heater inlet temperature and flow rate, as well as the inlet water temperature, pressure, and flow rate of the 8# LTH, were used as input variables. The LLTE inlet temperature, Fgot, air heater inlet water temperature, return 6# LTH temperature, and air outlet temperature were selected as output targets for validation. The accuracy of the model was verified by comparing the simulated outputs with the experimental values. To ensure the model's reliability, three operating conditions—high load, medium load, and variable load—were analyzed and validated, as shown in Fig. 13(b), (c), and (d).

The results indicated that the developed model possessed strong adaptability, with an overall error within 1 %. During the optimization process, 300 iterations were performed, and the model converged after 200 iterations, further confirming its robustness and reliability.

Fig. 14 presents the variations of the LLTE and AR inlet and outlet parameters. As shown in Fig. 14(a), from 19:00–24:00, the experiment's average flue gas outlet temperature was 89.95℃, while the optimized FGT was 88.24℃, reflecting a temperature drop of 1.70℃. In Fig. 14(b), the average AR outlet temperature during the experiment was 101.52℃, whereas the optimized average reached 106.19℃, showing a 4.67℃ increase. The rise in AR outlet temperature further enhanced boiler efficiency, increasing the system's output power.

This finding is consistent with the conclusion of Li et al. (2023), who reported that the increase in output power after introducing the LLTE was primarily attributed to the higher preheated air temperature. At this stage, the extraction steam from the low-pressure turbine was significantly reduced, which enhanced the turbine's power output and lowered coal consumption. Under the current design, the power output reaches 1024.28 MW, achieving a coal saving of 3.69 g/kWh.

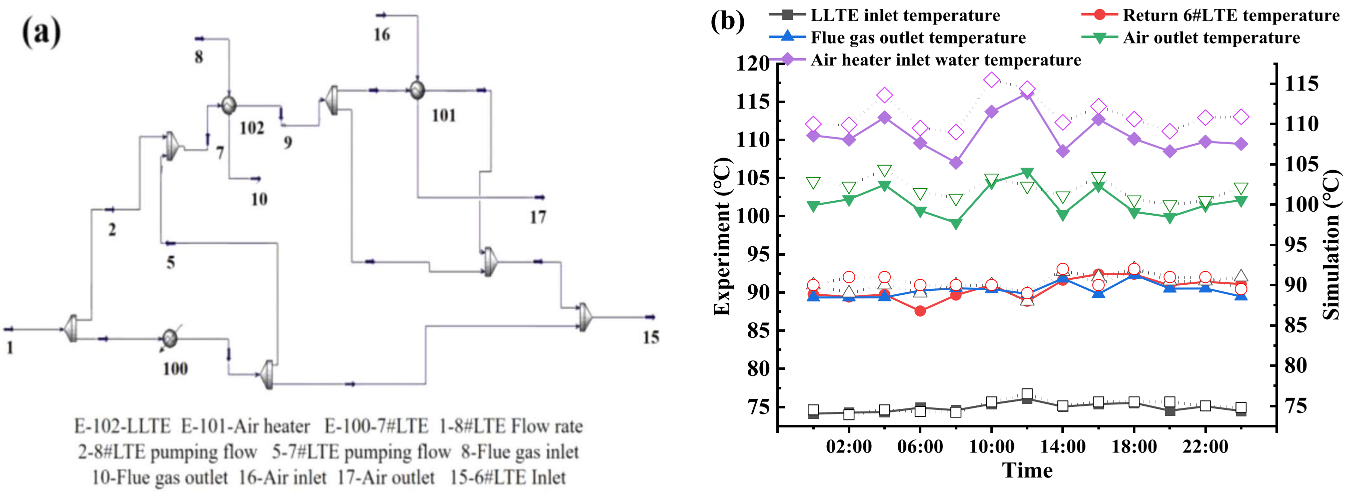

(a) HYSYS Model

(b) Model Validation- Variable load

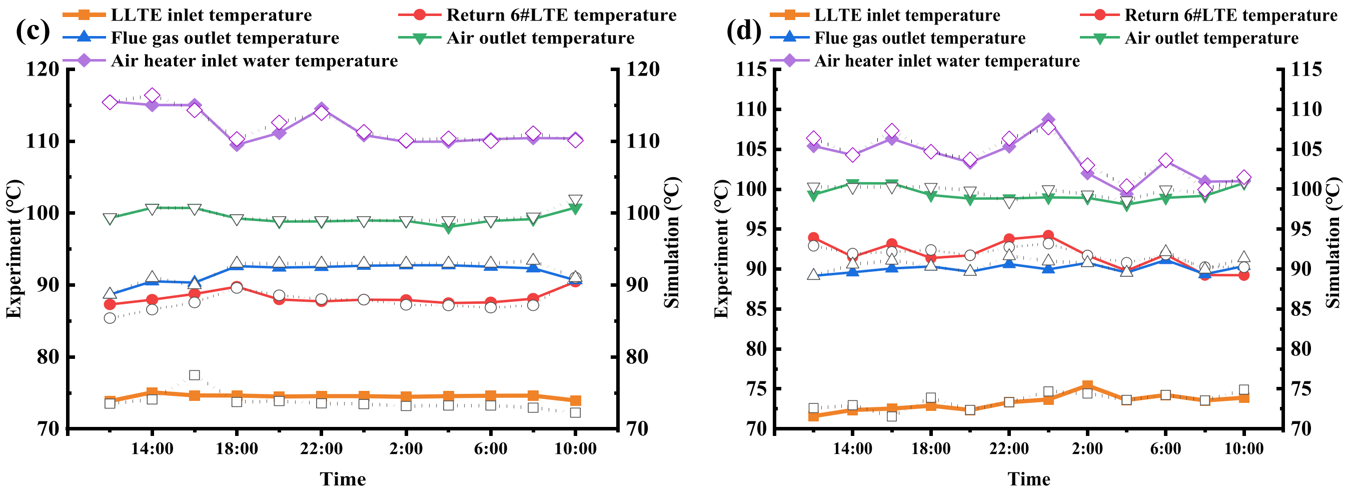

(c) Model Validation-High load

(d) Model Validation- Medium load

Fig. 13. Hysys model verification and CPO-HYSYS algorithm flow chart.

As illustrated in Fig. 14(c), the water temperatures at the LLTE inlet were almost the same for both the experiment and optimization. However, the optimized outlet water temperature after heating by the LLTE was noticeably higher than the experimental result. Additionally, in Fig. 14(d), it is evident that the optimized LLTE inlet flow rate was greater than the experimental value, with the optimized average flow rate being 603.49 kg/s compared to the experimental average of 536.07 kg/s.

Notably, the outlet temperatures of the AR and flue gas showed opposite patterns. At 21:15, the FGT dropped to its lowest point of 89.12℃, while the optimized AR outlet temperature reached a peak of 109.73℃. Because the increased total water flow into the AR following optimization. After optimization, the total water flow into the AR increased, and the relatively low FGT at 21:15 limited available waste heat. To meet system demands, the inlet temperature of the LLTE cooling medium was raised because of the advantage of lowering the FGT. A reduced outlet temperature enhanced the system's overall WHR, enabling more cold water to be heated.

Fig. 15 illustrates the energy variation relationship between the LLTE and the AR. At 21:15, the FGT reached its lowest point, resulting in the minimum FGWHR. As the FGT gradually increased, the optimized utilization of additional waste heat peaks at 22:15. During this period, the average experimental FGWHR was 77.07 MW, with a maximum of 84.14 MW and a minimum of 72.61 MW. Following optimization, the maximum, minimum, and average values of the additionally FGWHR increased by 2.51 MW, 1.04 MW, and 1.72 MW, respectively.

At 21:45, the AR greatly increased additional waste heat utilization. Fig. 14(d) shows that the optimized system supports a higher heat transfer water flow during this period, resulting in increased AR outlet temperature and improved WHR. During this time, the WHR by the AR reached a maximum of 46.36 MW, a minimum of 40.71 MW, and an average of 53.52 MW. After optimization, the additional heat recovered by the AR increased by 4.35 MW at maximum, 1.26 MW at minimum, and 2.63 MW on average. Exergy lost in the LLTE and AR increased with heat absorption. After optimization, higher cold-water flow and greater temperature differences caused exergy losses to rise.

Fig. 16 shows that thermal efficiency rises with work output per kg of coal, closely matching the FGWHR trend. Eqs. (8) and (9) show that the increase in thermal efficiency depended on work per kg of coal and FGWHR, while extra work mainly depended on the flue gas enthalpy difference and WHR of AR. The combined influence of these factors resulted in the lowest optimized value of 102.92 kJ/kg at 21:15, and the highest value of 116.95 kJ/kg at 19:45. Additional work per kg of coal averaged 108.95 kJ/kg, 12.56 kJ/kg more than the experimental value. After optimization, the thermal efficiency increased, peaking at 0.9971 % at 19:45, and was more stable than the experimental data. The

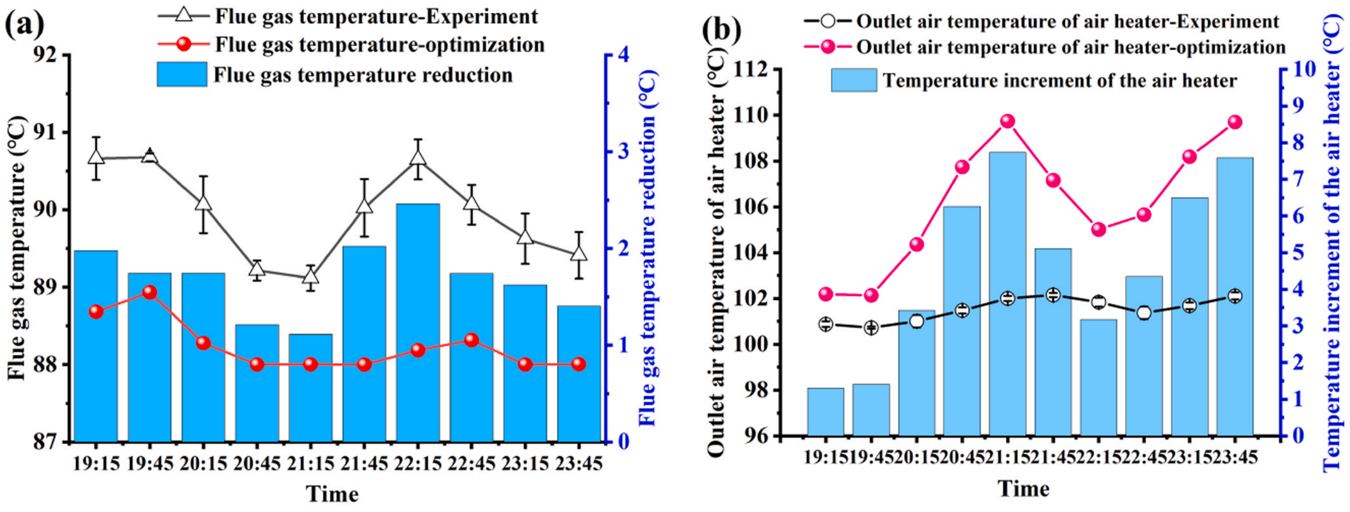

(a) Comparison of Flue Gas Outlet Temperature

(b) Comparison of Outlet Air Temperature

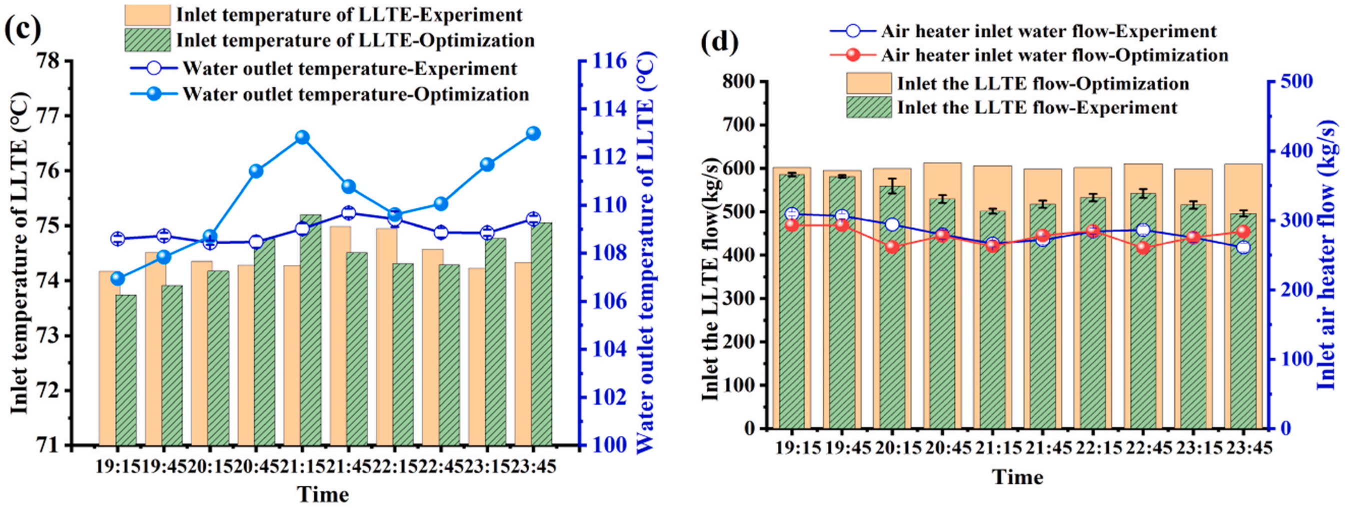

(c) Comparison of Water Temperature

(d) Comparison of Flow Rate

Fig. 14. Variation of LLTE and AR parameters.

optimized thermal efficiency rose by 0.93 % on average, 0.109 % higher than the experiment.

After optimization, the system exhibited a lower FGT, enabling more effective FGWHR from the boiler's exhaust. This recovered heat was utilized to preheat feedwater, condensate, and cold secondary air, thereby reducing the additional thermal energy required by the boiler to maintain steam production. As a result, the system's thermal efficiency was further improved, leading to increased power output and reduced coal consumption.

At present, the utilization of low-temperature flue gas waste heat in coal-fired units mainly focused on the design of thermodynamic systems. For instance, Yan et al. (2018) coupled bypass-LLTE technology with heat pump systems to achieve stepwise utilization of flue gas, reducing coal consumption by 5.38 g/kWh, which was 1.76 g/kWh more than that of a standalone bypass-LLTE system. Similarly, Ma et al. (2021) exploited the phase-change heat transfer characteristics of lithium bromide solution, efficiently recovering flue gas waste heat through evaporation and condensation processes and applying it to preheat combustion air. By dynamically adjusting the concentration of the lithium bromide solution, the system was ensured to operate efficiently under various working conditions.

Fig. 17 illustrates the variations in coal savings and CO_2 emission reductions. The amount of coal saved primarily depended on the improvement in boiler thermal efficiency and the system load. A higher load corresponded to a more significant value of b_0, while the optimized thermal efficiency improvement remained relatively stable.

Since the power output at 19:45 was 952.06 kW, significantly higher than the 875.32 kW recorded at 21:15, the coal savings reached a minimum of 2.02 g/kWh at 21:15 and a maximum of 2.46 g/kWh at 19:45, corresponding to approximately 75.65 % and 92.13 % of the rated load, respectively. The largest coal savings of 0.26 g/kWh occurred at 21:15, representing an improvement of approximately 10.86 %, when both the extra work per kilogram of coal WHR exhibited their greatest enhancements compared with the experimental data.

According to Eq. (16), CO_2 emission reduction was primarily determined by the savings in coal consumption and the output power. After optimization, the maximum CO_2 reduction was achieved at 19:45, reaching 8.5 t/h, while the minimum was observed at 21:15 at 6.1 t/h, corresponding to approximately 82.5 % and 59.14 % of the rated load, respectively. Overall, the optimized system achieved an average CO_2 reduction of 0.81 t/h.

To verify the impact of the optimization scheme on the economic performance of coal-fired units, the most important economic indicators were selected —coal savings and the incremental work output per

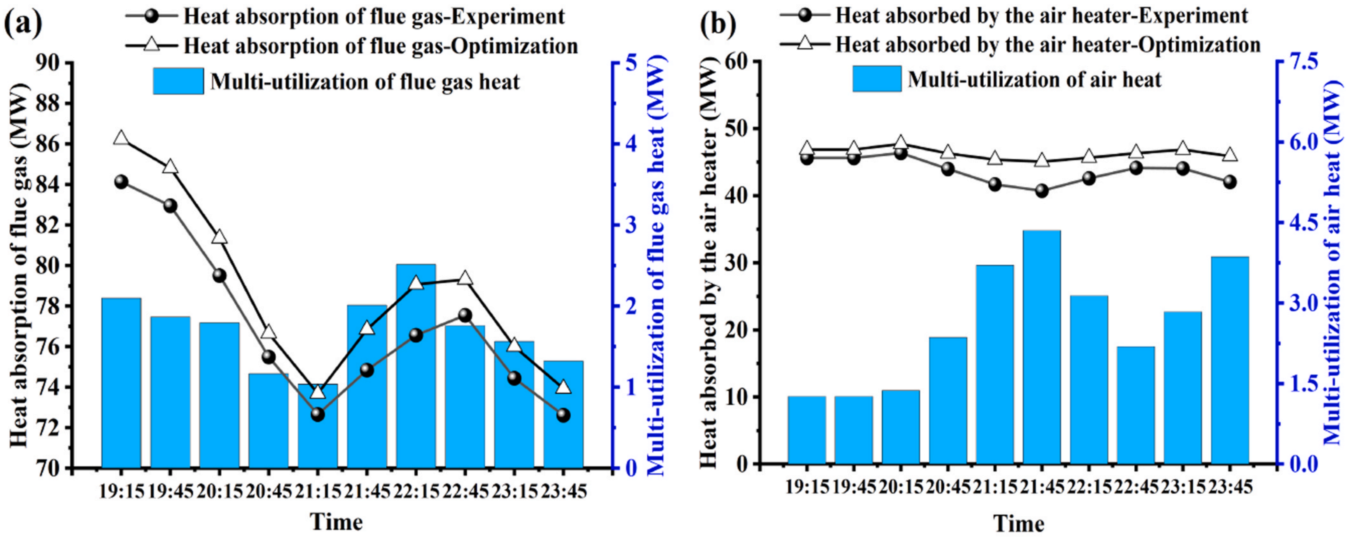

(a)Comparison of FGWHR

(b) Comparison of Heat Absorption by the AR

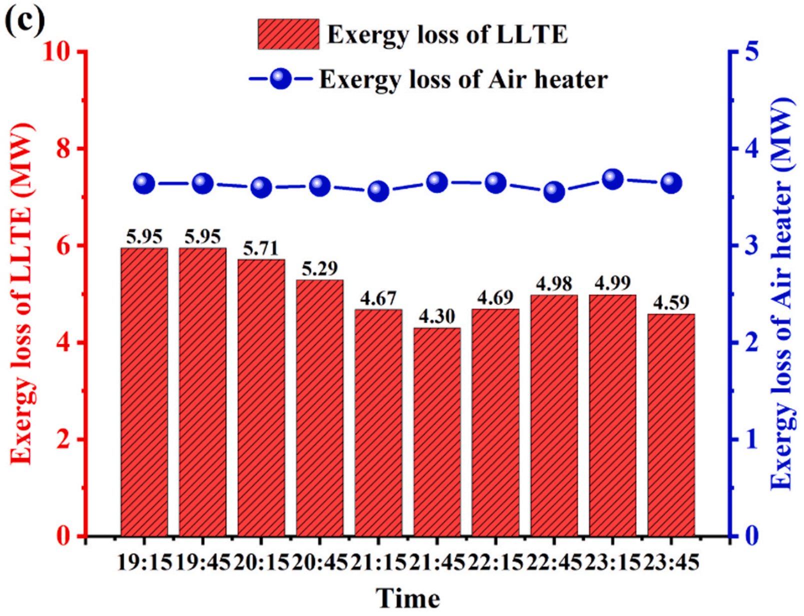

(c) Exergy Analysis

Fig. 15. Energy changes of LLTE and AR.

kilogram of coal—for comparative statistical analysis before and after optimization. Statistical analyses, including Analysis of Variance, independent-sample t-tests, effect size calculations, and Welch's t-tests, were conducted for validation. The results were presented in Tables 4 and 5.

The results showed that the optimized scheme significantly reduced coal consumption while markedly increased the work output per kilogram of coal. Independent-sample t-tests confirmed that the differences were highly statistically significant. The calculated Cohen's d values of 1.56 and 2.36 further demonstrated that the optimization substantially lowered coal consumption and enhanced the incremental work output. Moreover, the consistency between the Analysis of Variance and Welch's *t*-test results provided additional support for the robustness of these findings. Overall, the proposed optimization scheme effectively reduced coal consumption and increased work output per kilogram of coal without compromising unit performance, and thus offered practical value for energy saving and emission reduction in coal-fired power plants.

7. Conclusions

The capacity expansion of a 1000 MW supercritical unit through the integration of a low-temperature economizer (LLTE) and a secondary air heater (AR) was investigated. By combining thermodynamic analysis with intelligent algorithms, the nonlinear behavior and time-delay characteristics of the LLTE flue gas–water heat exchange system under variable load conditions were addressed.

The results demonstrated that the LLTE system effectively recovered low-temperature flue gas waste heat to preheat both feedwater and secondary air, thereby lowering flue gas temperature, reducing coal

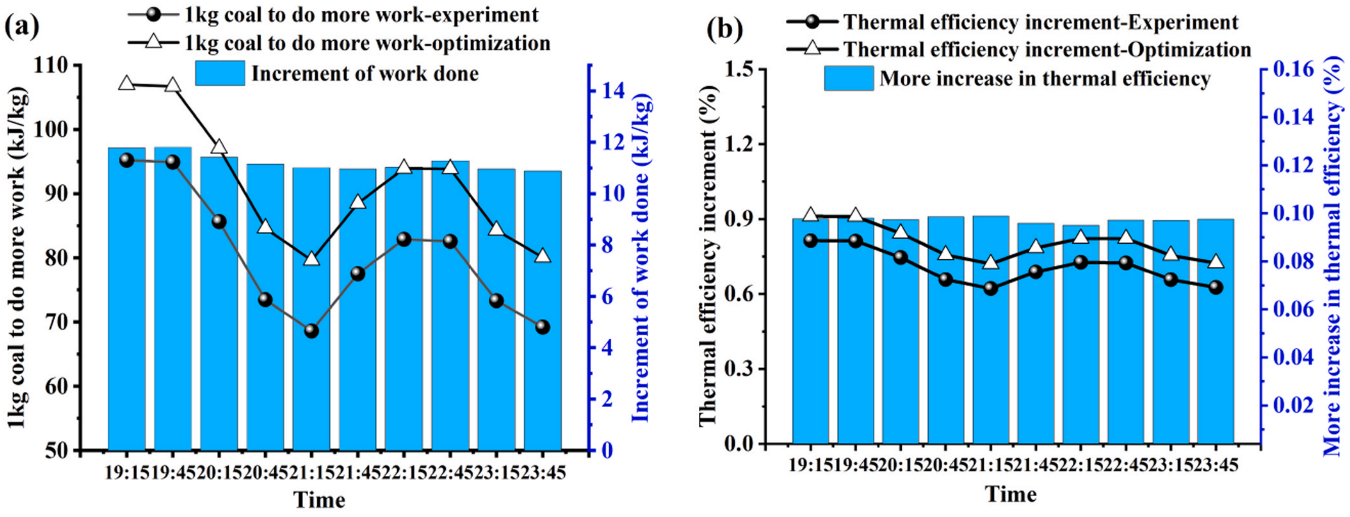

(a) Comparison of Work Output per Kilogram

(b) Comparison of Thermal Efficiency Increment

Fig. 16. Thermal efficiency increment and 1 kg coal work change.

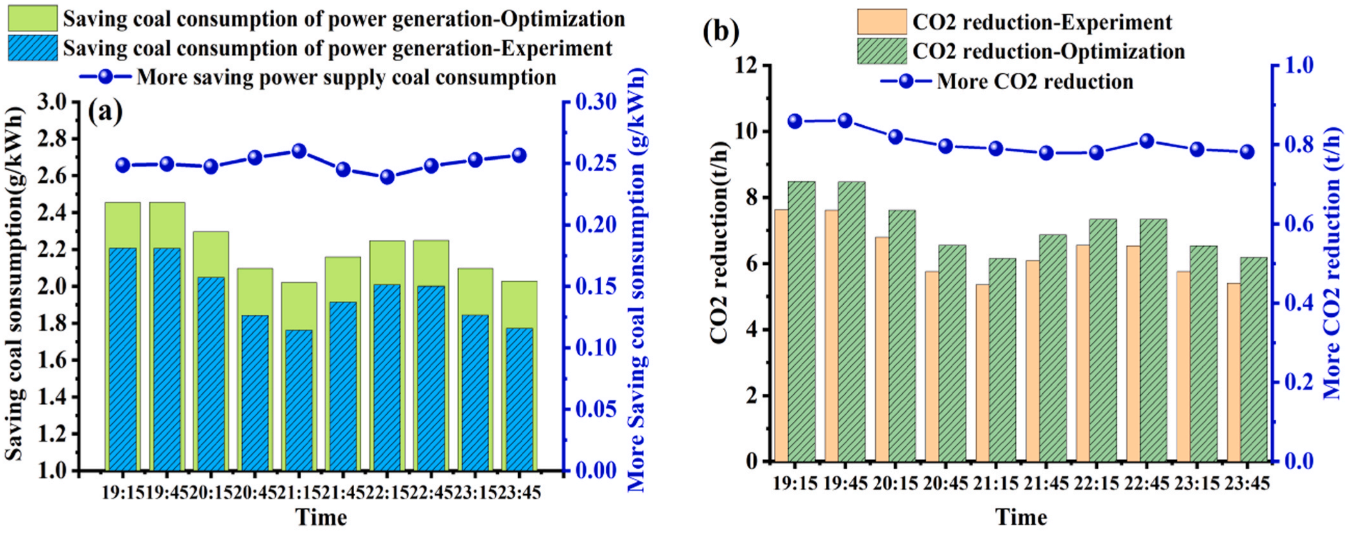

(a) Saved coal consumption

(b) CO₂ emission reduction

Fig. 17. Economic analysis.

Table 4
Increased work output per kilogram of coal.

Analysis of Variance	F(1,18) = 27.79	p = 0.0001
Independent Samples *t*-test Welch *t*-test Cohen’s d	t(18) = −5.27 t(1.790119e+01)= −5.27 2.36	p_t= 0.0001 p_{welch}= 0.0001

Table 5
Coal consumption savings.

Analysis of Variance	F(1,18) = 12.14	p = 0.0027
Independent Samples *t*-test Welch *t*-test Cohen’s d	t(18) = −3.48 t(1.799139e+01)= −3.48 1.56	p_t = 0.0027 p_{welch} = 0.0027

consumption, and improving overall plant efficiency. The application of the Chaotic Particle Optimization-Least Squares Support Vector Machine (CPO-LSSVM) model further ensured accurate flue gas parameter prediction, which enhanced the stability and efficiency of the optimization process. In addition, the CPO-HYSYS model verified that coordinated system optimization can achieve tangible improvements in energy efficiency and environmental performance, highlighting the potential of LLTE–AR integration for large-scale coal-fired units.

The technical and economic feasibility of LLTE and AR retrofitting in supercritical units was validated but also provides a systematic methodology for intelligent prediction and optimization. Future research will further explore coordinated energy distribution strategies between the LLTE, cogeneration system, and AR, aiming to maximize efficiency gains while promoting sustainable power generation.

Financial support

This work was supported by the Fundamental Research Funds for the Central Universities (2022ZFJH04).

CRediT authorship contribution statement

Hao Zhou: Supervision, Project administration. **Tianxing Zhou:** Software. **Yajie Wu:** Validation, Formal analysis. **Dongliang Wei:** Writing – review & editing, Methodology, Data curation. **Huaan Li:** Writing – original draft, Methodology, Investigation, Data curation, Conceptualization.

Declaration of Competing Interest

The authors declare that they have no known competing financial interests or personal relationships that could have appeared to influence the work reported in this paper.

Data Availability

All data that support the findings of this study are included in this manuscript and its supplementary information files

References

Abbas, W.K.A., Vrabec, J., 2021. Cascaded dual-loop organic rankine cycle with alkanes and low global warming potential refrigerants as working fluids. Energy Convers. Manag. 249, 114843.

Abdel-Basset, M., Mohamed, R., Abouhawwash, M., 2024. Crested porcupine optimizer: a new nature-inspired metaheuristic. Knowl. Based Syst. 284, 111257.

Bao, Y., Zhou, H., Li, J., 2024. Physics-based machine learning optimization of thermoelectric assembly for maximizing waste heat recovery. Energy 307, 132821.

Bellos, E., 2024. Thermodynamic analysis of a carnot battery unit with double exploitation of a waste heat source. Energy Convers. Manag. 299, 117844. https://doi.org/10.1016/j.enconman.2023.117844.

Caliskan, H., Gurbuz, H., Sohret, Y., Ates, D., 2022. Thermal analysis and assessment of phase change material utilization for heating applications in buildings: a modelling. J. Energy Storage 50, 104593. https://doi.org/10.1016/j.est.2022.104593.

Chen, Y., Lu, C., Tian, S., Gu, Q., Jiang, S., Li, X., Zou, Y., 2023. Monitoring and detecting coal miners' fatigue status using MPA-LSSVM in the vision of smart mine. Process Saf. Environ. Prot. 179, 774–783. https://doi.org/10.1016/j.psep.2023.09.054.

Comak, E., Polat, K., Güneş, S., Arslan, A., 2007. A new medical decision making system: least square support vector machine (LSSVM) with fuzzy weighting pre-processing. Expert Syst. Appl. 32 (2), 409–414.

Di Bonito, L.P., Campanile, L., Napolitano, E., Iacono, M., Portolano, A., Di Natale, F., 2023. Analysis of a marine scrubber operation with a combined analytical/AI-based method. Chem. Eng. Res. Des. 195, 613–623.

Dong, S., Hu, X., Huang, J.F., Zhu, T., Zhang, Y., Li, X., 2021. Investigation on improvement potential of ORC system off-design performance by expander speed regulation based on theoretical and experimental exergy-energy analyses. Energy 220, 119753.

Espatolero, S., Cortés, C., Romeo, L.M., 2010. Optimization of boiler cold-end and integration with the steam cycle in supercritical units. Appl. Energy 87 (5), 1651–1660.

Feng, Y.-q, Liang, H.-j, Xu, K., Wang, Y., Lu, Y., Lin, C.-H., Hung, T.-C., 2023. Experimental study on the performance of a great progress 10 kw organic rankine cycle for low-grade heat source based on scroll-type expander. Energy 284, 128627.

Gürbüz, H., 2018. The effect of H2 purity on the combustion, performance, emissions and energy costs in an SI engine, 315 Therm. Sci. 24, 315. https://doi.org/10.2298/TSCI180705315G.

Gürbüz, H., Aytaç, H.E., Akçay, H., Cahit Hamamcıoğlu, H., 2022. Improvement of volume controlled thermal energy storage system using phase change material for exhaust waste heat recovery in a SI engine. J. Energy Storage 53, 105107. https://doi.org/10.1016/j.est.2022.105107.

Gürel, B., Kurtuluş, K., Yurdakul, S., Varol, M., Keçebaş, A., Gürbüz, H., 2023. Numerical and experimental investigation of co-combustion of chicken manure and lignite blends in a CFBB with novel compact combustion chamber. Energy 285, 129482. https://doi.org/10.1016/j.energy.2023.129482.

Gürel, B., Kurtuluş, K., Yurdakul, S., Karaca Dolgun, G., Akman, R., Önür, M.E., Gürbüz, H., 2024. Combustion of chicken manure and turkish lignite mixtures in a circulating fluidized bed. Renew. Sustain. Energy Rev. 189, 113960. https://doi.org/10.1016/j.rser.2023.113960.

He, Z., Liu, P., Zhao, X., He, X., Liu, J., Mu, Y., 2022. Responses of surface O3 and PM2. 5 trends to changes of anthropogenic emissions in summer over Beijing during 2014–2019: a study based on multiple linear regression and WRF. Chem. Sci. Total Environ. 807, 150792.

Jiang, Y., Su, W., Wu, C., Wang, S., 2024. Enhanced thermally integrated carnot battery using low-GWP working fluid pair: Multi-aspect analysis and multi-scale optimization. Appl. Energy 376, 124226. https://doi.org/10.1016/j.apenergy.2024.124226.

Jiang, Y., Wang, S., Wang, Z., Su, W., 2024. Performance enhancement of gas turbine by supercritical CO2 cycle construction: system and component two-level evaluation. Energy 302, 131830. https://doi.org/10.1016/j.energy.2024.131830.

Kadkhodazadeh, M., Farzin, S., 2021. A novel LSSVM model integrated with GBO algorithm to assessment of water quality parameters. Water Resour. Manag. 35 (12), 3939–3968.

Kehlhofer, R. ,1991. Combined-cycle gas and steam turbine power plants.

Li, Y., Chen, X., Jiang, S., Lu, G., 2023. Thermodynamics of cascaded waste heat utilization from flue gas and circulating cooling water. J. Therm. Sci. 32 (6), 2166–2178.

Li, H., Wei, D., Wu, Y., Li, H., Liu, H., Hu, X., Zhou, H., 2025. Advanced optimization of thermal efficiency in low-low temperature economizers and air heater system employing the crested porcupine optimizer algorithm. Expert Syst. Appl. 290, 128352. https://doi.org/10.1016/j.eswa.2025.128352.

Lin, C.-H., Hsu, P.-P., He, Y.-L., Shuai, Y., Hung, T.-C., Feng, Y.-Q., Chang, Y.-H., 2019. Investigations on experimental performance and system behavior of 10 kw organic rankine cycle using scroll-type expander for low-grade heat source. Energy 177, 94–105.

Liu, Y., Han, J., You, H., 2020. Exergoeconomic analysis and multi-objective optimization of a CCHP system based on LNG cold energy utilization and flue gas waste heat recovery with CO2 capture. Energy 190, 116201.

Lu, X., Sha, Y.H., Li, Z., Huang, Y., Chen, W., Chen, D., Fung, J.C.H., 2021. Development and application of a hybrid long-short term memory–three dimensional variational technique for the improvement of PM2. 5 forecasting. Sci. Total Environ. 770, 144221.

Lu, D., Xu, Q., Chen, G., Dong, X., Bai, Y., Gong, M., Shen, J., 2019. Modeling and analysis of an ammonia–water absorption refrigeration system utilizing waste heat with large temperature span. Int. J. Refrig. 103, 180–190.

Ma, H., Liang, N., Liu, Y., Luo, X., Hou, C., Wang, G., 2021. Experimental study on novel waste heat recovery system for sulfide-containing flue gas. Energy 227, 120479.

Men, Y., Liu, X., Zhang, T., 2021. A review of boiler waste heat recovery technologies in the medium-low temperature range. Energy 237, 121560.

Ouyang, T., Xu, J., Su, Z., Zhao, Z., Huang, G., Mo, C., 2021. A novel design of low-grade waste heat utilization for coal-fired power plants with sulfuric acid recovery. Energy Convers. Manag. 227, 113640.

Pan, S., Shi, X., Dong, B., Skvaril, J., Zhang, H., Liang, Y., Li, H., 2024. Multivariate time series prediction for CO2 concentration and flowrate of flue gas from biomass-fired power plants. Fuel 359, 130344.

Qi, Y.-P., He, P.-J., Lan, D.-Y., Lü, F., Zhang, H., 2025. Novel method for predicting concentrations of incineration flue gas based on waste composition and machine learning. J. Environ. Manag. 373, 123588.

Qiao, H., Yu, X., Yang, B., 2023. Working fluid design and performance optimization for the heat pump-organic rankine cycle carnot battery system based on the group contribution method. Energy Convers. Manag. 293, 117459.

Sang, B., 2021. Application of genetic algorithm and BP neural network in supply chain finance under information sharing. J. Comput. Appl. Math. 384, 113170.

Shi, L., Shu, G., Tian, H., Deng, S., 2018. A review of modified organic rankine cycles (ORCs) for internal combustion engine waste heat recovery (ICE-WHR). Renew. Sustain. Energy Rev. 92, 95–110.

Singh, P.K., Basem, A., Dara, R.N., Shaban, M., Samad, S., Ghandour, R., Alsayer, I.A., 2024. Waste heat recovery cycles integration into a Net-Zero emission solar-thermal multi-generation system; techno-economic analysis and ANN-MOPSO optimization. Case Stud. Therm. Eng., 105690

Stevanovic, V.D., Petrovic, M.M., Wala, T., Milivojevic, S., Ilic, M., Muszynski, S., 2019. Efficiency and power upgrade at the aged lignite-fired power plant by flue gas waste heat utilization: high pressure versus low pressure economizer installation. Energy 187, 115980.

Stevanovic, V.D., Wala, T., Muszynski, S., Milic, M., Jovanovic, M., 2014. Efficiency and power upgrade by an additional high pressure economizer installation at an aged 620 MWe lignite-fired power plant. Energy 66, 907–918.

Sun, X., Liu, L., Zhang, T., Dai, Y., 2024. Multi-objective optimization of a rectisol process integrated with compression-absorption cascade refrigeration system and ORC for waste heat recovery. Appl. Therm. Eng. 244, 122611.

Tang, H., Liu, M., Zhang, K., Zhang, S., Wang, C., Yan, J., 2024. Performance evaluation and operation optimization of a combined heat and power plant integrated with molten salt heat storage system. Appl. Therm. Eng. 245, 122848.

Tassenoy, R., Dumont, O., Lemort, V., De Paepe, M., Lecompte, S., 2022. Experimental investigation of a thermally integrated carnot battery using a reversible heat pump/organic rankine cycle: influence of system charge on performance of the reversible scroll compressor/expander and global performance. School Mech. Eng.

Tavana, M., Deymi-Dashtebayaz, M., Gholizadeh, M., Ghorbani, S., Dadpour, D., 2024. Optimizing building energy efficiency with a combined cooling, heating, and power (CCHP) system driven by boiler waste heat recovery. J. Build. Eng. 97, 110982.

Tresp, V., 2001. Scaling kernel-based systems to large data sets. Data Min. Knowl. Discov. 5 (3), 197–211.

Wang, C., He, B., Sun, S., Wu, Y., Yan, N., Yan, L., Pei, X., 2012a. Application of a low pressure economizer for waste heat recovery from the exhaust flue gas in a 600 MW power plant. Energy 48 (1), 196–202.

Wang, C., He, B., Sun, S., Wu, Y., Yan, N., Yan, L., & Pei, X.J.E. ,2012b. Application of a low pressure economizer for waste heat recovery from the exhaust flue gas in a 600 MW power plant. *48*(1), 196-202.

Wang, C., He, B., Yan, L., Pei, X., & Chen, S.J.E. ,2014. Thermodynamic analysis of a low-pressure economizer based waste heat recovery system for a coal-fired power plant. *65*, 80-90.

Wang, Z., Zhang, X., Han, J., Li, Z., 2017. Waste heat and water recovery from natural gas boilers: parametric analysis and optimization of a flue-gas-driven open absorption system. Energy Convers. Manag. 154, 526–537.

Wang, Q., Zhao, H., Zhao, Q., Hou, J., Tian, S., Li, Y., Gu, J., 2024. Prediction of SO2 emission concentration in industrial flue gas based on deep learning: the ammonia desulfurization system of the yunnan aluminum carbon plant as the research object. Process Saf. Environ. Prot. 185, 340–349.

Xiao, P., Zhang, Y., Wang, Y., Wang, J., 2019. Analysis of an improved economizer system for active control of the coal-fired boiler flue gas temperature. Energy 170, 185–198.

Xu, W., Jin, Y., Zhu, L., Li, Z., 2021. Performance analysis of the technology of High-Temperature boiler feed water to recover the waste heat of Mid-Low-Temperature flue gas. ACS Omega 6 (40), 26318–26328 (In).

Yan, M., Zhang, L., Shi, Y., Zhang, L., Li, Y., Ma, C., 2018. A novel boiler cold-end optimisation system based on bypass flue in coal-fired power plants: heat recovery from wet flue gas. Energy 152, 84–94.

Yuan, X., Liang, Y., Hu, X., Xu, Y., Chen, Y., Kosonen, R., 2023. Waste heat recoveries in data centers: a review. Renew. Sustain. Energy Rev. 188, 113777.

Zhang, B., Rong, Y., Yong, R., Qin, D., Li, M., Zou, G., Pan, J., 2022. Deep learning for air pollutant concentration prediction: a review. Atmos. Environ. 290, 119347.

Zhang, G., Zhang, S., Sun, B., Liu, J., Yan, J., 2024. Design on a novel waste heat recovery system integrated with the bypass flue and outside primary air preheater for bitumite-fired power plants. Energy 291, 130341.

Zhao, Z., Zhang, Y., Gao, W., Baleta, J., Liu, C., Li, W., Gao, X., 2021. Simulation of SO2 absorption and performance enhancement of wet flue gas desulfurization system. Process Saf. Environ. Prot. 150, 453–463.

Zoghi, M., Hosseinzadeh, N., Gharaie, S., Zare, A., 2024. 4E optimization comparison of different bottoming systems for waste heat recovery of gas turbine cycles, internal combustion engines, and solid oxide fuel cells in power-hydrogen production systems. Process Saf. Environ. Prot. 187, 549–580.